Comptes Rendus

Géoscience

Sciences de la Planète

Anne Paul, Helle A. Pedersen, Thomas Bodin, Emanuel Kästle, Dorian Soergel, Chloé Alder, Yang Lu and Ahmed Nouibat

Methodological advances in seismic noise imaging of the Alpine area

ACADÉMIE
DES SCIENCES
INSTITUT DE FRANCE

Research article

New Developments in Passive Seismic Imaging and Monitoring

Methodological advances in seismic noise imaging of the Alpine area

Anne Paul [ORCID],[*],[a]**, Helle A. Pedersen** [ORCID],[a]**, Thomas Bodin** [ORCID],[b]**, Emanuel Kästle** [ORCID],[c]**,
Dorian Soergel [ORCID],[a]**, Chloé Alder** [ORCID],[b]**, Yang Lu** [ORCID],[a] **and Ahmed Nouibat** [ORCID],[a]

[a] Univ. Grenoble Alpes, Univ. Savoie Mont Blanc, CNRS, IRD, UGE, ISTerre, Grenoble, France

[b] Univ. Lyon, Univ. Lyon 1, ENSL, UJM-Saint-Etienne, CNRS, LGL-TPE, F-69622, Villeurbanne, France

[c] Institute of Geological Sciences, Freie Universität Berlin, Berlin, Germany

Current addresses: Berkeley Seismological Laboratory, University of California, Berkeley, CA 94720, USA (D. Soergel), Department of Meteorology and Geophysics, University of Vienna, Vienna, Austria (Y. Lu), ITES-EOST, CNRS/Université de Strasbourg, 67000 Strasbourg, France (A. Nouibat)

E-mails: anne.paul@univ-grenoble-alpes.fr (A. Paul), helle.pedersen@univ-grenoble-alpes.fr (H. A. Pedersen), thomas.bodin@ens-lyon.fr (T. Bodin), emanuel.kaestle@fu-berlin.de (E. Kästle), soergeldorian@gmail.com (D. Soergel), chloe.alder@gmx.fr (C. Alder), yang.lu@univie.ac.at (Y. Lu), ahmed.nouibat@univ-grenoble-alpes.fr (A. Nouibat)

Abstract. Methodological advances in seismic tomography are often driven by the quality of data sets. The dense and homogeneous spatial coverage of the AlpArray seismic network, including hundreds of permanent and temporary broadband stations, has motivated a series of methodological developments of ambient-noise-based tomography of the lithosphere across the entire Alps-Apennines regions, which have been published and are reviewed here. To take full advantage of the ocean-bottom seismometers (OBS) in the Ligurian-Provence basin, reconstructed Rayleigh wave signals between OBS have been improved by second-order correlations with onland stations. A Bayesian or fully transdimensional formalism has been introduced in both steps of isotropic ambient noise tomography. The three-dimensional S-wave velocity models have been further improved by wave-equation based inversions accounting for the physics of seismic wave propagation, including elastic–acoustic coupling at the sea bottom. A beamforming approach has been developed to avoid systematic errors in the measurement of azimuthal anisotropy from seismic noise. Probabilistic inversions for depth variations of azimuthal and radial anisotropy have provided robust estimates of anisotropic parameters in the crust and upper mantle that differ significantly from earlier surface-wave tomography studies. These methodological improvements have taken the full benefit of the quality of available seismic data to significantly improve knowledge of the seismic structure of the crust and shallow mantle beneath the Alps-Apennines system. Our findings include detailed mapping of strong and abrupt Moho depth changes under the Western Alps, contrasting orientations of fast velocity directions between the upper and lower Alpine crust, and the absence of significant radial anisotropy everywhere in the European

[*]Corresponding author

crust and shallow upper mantle, except in the Apenninic lower crust. These methods can be applied to similar dense arrays with equivalent potential benefits.

1. Introduction

The Alpine mountain range is part of the continental collision ranges created by the convergence of the Eurasian and African plates in the Mediterranean region. It results from the subduction of the Alpine Tethys under the Adriatic microplate since the Late Cretaceous, and the subsequent continental collision between the European and Adriatic paleomargins in the Cenozoic [e.g., Handy et al., 2010]. The Alpine belt is an outstanding example of subduction and continental collision studies, which has been investigated by geologists for more than 150 years. Several major concepts of modern geology have been developed in the Alps, such as nappes, when the prominence of horizontal over vertical displacements was proposed by Emile Argand [Argand, 1922]. More recently, the identification of coesite, which is a high-pressure polymorph of quartz, in gneisses of the Dora Maira massif (south-western Alps, Italy) led Chopin [1984] to propose that continental crust may be subducted to depths of 90 km or more. The amount of geological knowledge about the Alps is unparalleled in any other mountain range, and they provide a unique natural laboratory to advance our understanding of orogenesis and its relationship to present and past mantle dynamics. The Alpine mountain belt is also a populated area where millions of Europeans are affected by its topography, geology and associated natural hazards such as earthquakes or landslides. Yet, accurate information on the lithospheric structure of that emblematic and populated mountain range was hampered by insufficient and spatially heterogeneous geophysical data until the last few years. Filling that gap was the primary motivation for the AlpArray initiative, which gathered a large number of European research institutions to deploy a dense and homogeneous temporary broadband seismological network over the Alps and its forelands to complement the permanent networks [Hetényi et al., 2018a].

In addition to gaining knowledge of Alpine lithospheric structure, the high spatial coverage of AlpArray temporary stations and permanent networks has given us the opportunity to develop new methods of seismic tomography at this large regional scale based on ambient noise. A review of these methodological developments is gathered in this paper because they could be applied with great benefit to other similar dense networks.

1.1. *Seismic imaging in the Alps*

Seismic imaging is an essential complement to geological studies to build lithospheric-scale interpretive models and improve the understanding of the dynamics of the mountain belt in space and time. The geometry and depth of the crust-mantle boundary, only accessible with geophysics and in particular active-source seismology and earthquake seismology, are key information for geological and geodynamic modeling. Each of these methods has limitations and provides partial information, which is why noise-based tomography methods are a valuable complement. In the Alps, deep seismic sounding (DSS) experiments including ECORS-CROP in the Western Alps [e.g., Nicolas et al., 1990], NFP-20 in the Central Alps [e.g., Frei et al., 1990], and TRANSALP in the Eastern Alps [e.g., Lüschen et al., 2006] provided crucial data for interpretive crustal-scale sections along a number of crooked lines mostly transverse to the belt. The results from these localised studies cannot be extrapolated to other locations along the belt due to its arcuate, non-cylindrical geometry. DSS profiles provide high-frequency reflectivity images of the crust, hence sharp and subhorizontal velocity contrasts with no or poor information on absolute velocities. Thus, they can-

not be interpreted in terms of petrology. Moreover, the European Moho, defined as the base of the highly reflective lower crust, was not detected below the intensely deformed and highly heterogeneous crust of the internal zones in the ECORS-CROP and NFP-20 W5 and E1 profiles across the Western and Central Alps [e.g., Nicolas et al., 1990, Marchant and Stampfli, 1997]. The deep European Moho has only been detected by the ECORS-CROP wide-angle seismic reflection experiment under part of the internal zones to a maximum depth of 55 km [ECORS-CROP Deep Seismic Sounding Group, 1989].

A similar type of information on velocity contrasts beneath seismic stations is provided at lower frequencies by receiver function (RF) analysis in particular for Moho depth estimates [e.g., Kummerow et al., 2004, Lombardi et al., 2008, Zhao et al., 2015, Hetényi et al., 2018b, Paul et al., 2022, Michailos et al., 2023]. In some specific cases, such as in the presence of a very heterogeneous, scattering crust, receiver function analysis can be more effective at detecting the crust-mantle boundary than reflection seismics because it uses low-frequency, high-energy waves from teleseismic earthquakes that travel across the heterogeneous crust only once. Moreover, receiver functions computed for station arrays provide estimates of Moho depth with 2-D coverage. Indeed, Spada et al. [2013] generated a Moho depth map of Italy, including the Alpine region, which combines DSS data with receiver functions. Spada et al. [2013]'s model displays three Moho surfaces, European, Adriatic-Ionian and Ligurian–Corsican–Sardinian–Tyrrhenian. As this model allows only one Moho at a given location, the Moho surfaces never overlap, even though the European lithosphere is known to underthrust Adria.

The polarity of converted waves in receiver functions provides useful information on the sign of velocity change with depth. For example, Zhao et al. [2015] observed negative-polarity P-to-S converted waves in RF of the CIFALPS profile close to the so-called Ivrea body positive Bouguer anomaly (blue line in Figure 1). This gravity anomaly high is known since the first geophysical experiments in the Alps that also reported high-velocity refracted waves (V_p = 7.4 km/s) at 10 km depth in the same area of the Italian Piemonte region [Closs and Labrouste, 1963]. The source of this gravity and seismic ve-

locity anomaly is called the Ivrea body and it is interpreted as a slice of Adriatic upper mantle at unusually shallow depth [e.g., Nicolas et al., 1990]. The negative-polarity converted phases in the RF of the CIFALPS profile were the first evidence for the inverted Moho beneath the Ivrea body, as the contact between the high-velocity Adriatic mantle wedge on top and the lower velocity European crust or subduction interface below [Zhao et al., 2015]. These negative-polarity converted waves from 20–60 km depth and the positive-polarity conversions at 75–80 km depth were the first seismic evidence for continental subduction of the European lithosphere beneath Adria, according to Zhao et al. [2015]. Like deep seismic sounding, however, receiver functions yield no clues on absolute velocities.

Local earthquake tomography (LET), which relies on the inversion of body-wave arrival times (mostly direct P and S waves) from local earthquakes for absolute velocities (V_p and V_s or V_p/V_s) is an efficient tool to get 3-D images and complement 2-D DSS or receiver function reflectivity images. The size of the imaged crustal volume and the resolution of the tomography depend on the distribution of seismic stations at the surface and earthquake hypocenters at depth. In the Alps, the seismicity level is low to moderate, with rare events of magnitude >5. Many years of recording are therefore required to reach sufficient ray coverage in local earthquake tomography studies of the whole Alpine region like in Diehl et al. [2009]: 12 years (1996–2007) for 1500 events of M_l > 2.5. Another issue is that most earthquake sources in the Alps are shallow (focal depths < 15 km), except in the westernmost part of the Po basin where hypocenters on the Rivoli-Marene fault reach 70–80 km depth [Eva et al., 2015]. Due to low magnitudes, these deep events are only detected by stations close to epicenters. They, however, proved useful to image the deep parts of the subduction wedge of the western Alps by LET including the high-velocity Ivrea body [Solarino et al., 1997, Paul et al., 2001, Solarino et al., 2018, Virieux et al., 2024]. Imaging the crust to Moho depth with LET in most of the Alps requires records of Pn waves, thus sufficient-magnitude earthquakes and station arrays of large spatial extent. Until recent years, this last condition was only reached by compiling records of a large number of regional and national networks with heterogeneous data sharing policies and traveltime picking strategies, at the cost
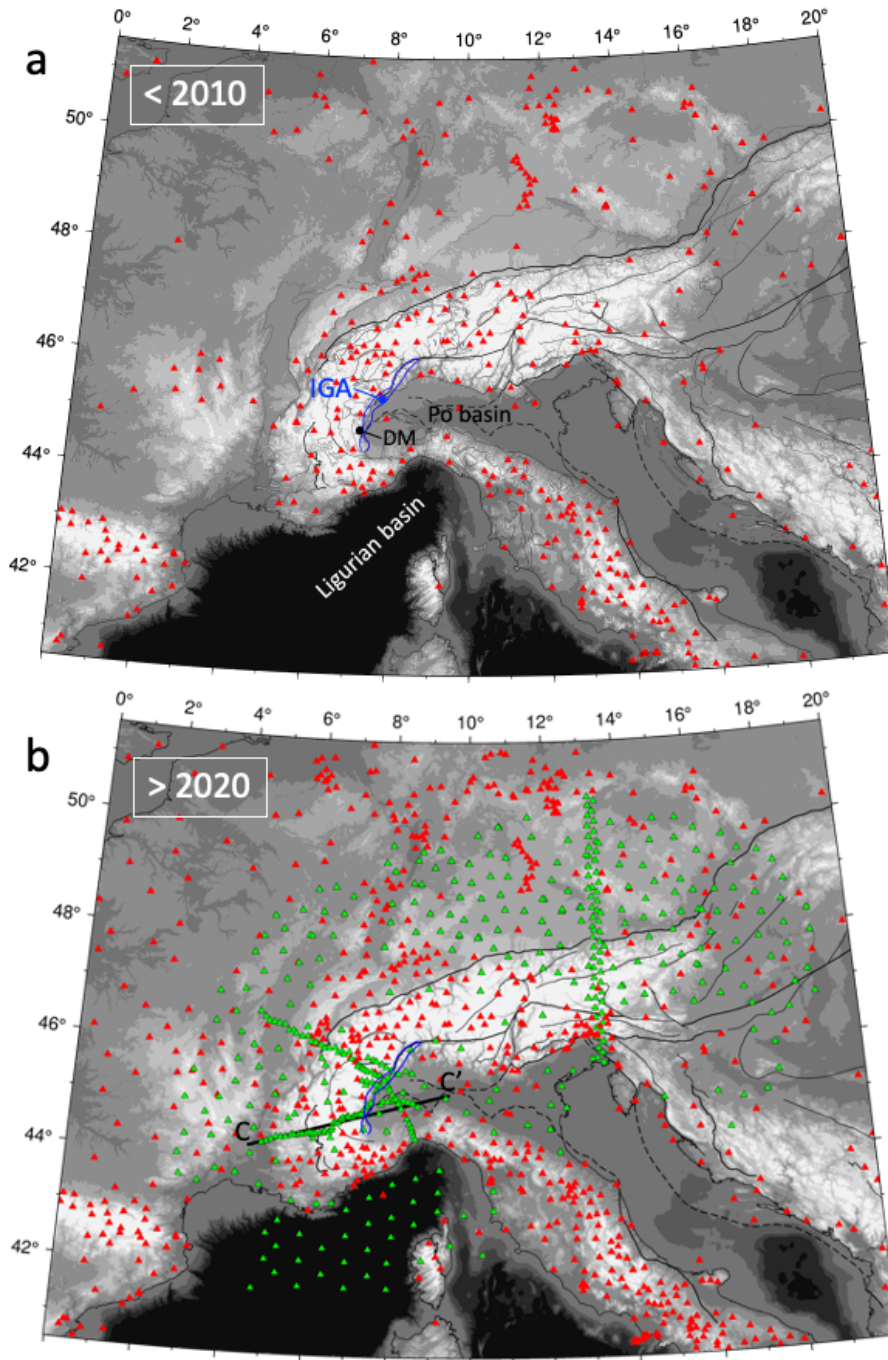
Figure 1. Maps of broadband seismic stations in the Alps and surrounding regions including all stations used in the studies discussed in Sections 2–3; (a) before 2010: red triangles are public permanent stations in 2009; (b) after 2020: red triangles are permanent stations in 2019; green triangles are temporary stations used in the studies described in this paper (EASI, AlpArray, CIFALPS and CIFALPS-2). The blue line in (a) and (b) is the 0 mgal contour of the Ivrea Bouguer anomaly. Black lines: main geological units and faults from the tectonic map compiled by M. R. Handy. The thick black line CC′ is the CIFALPS profile used in Figure 3. DM: Dora Maira massif; IGA: Ivrea gravity anomaly.

of heavy homogenization work [13 networks used in Diehl et al., 2009, Bagagli et al., 2022, and Virieux et al., 2024].

In addition to low-to-moderate seismicity and heterogeneous coverage of permanent seismic networks, the strong crustal heterogeneity and its very 3-D character are other challenges in seismic tomography of the Alpine lithosphere. Crustal heterogeneity is not surprising for a collisional belt with a long tectonic history. However, the arcuate shape of the western Alps, the presence of large and deep basins including the Po basin and its unconsolidated sediment layers and high level of anthropogenic noise close to the heart of the belt make seismic imaging of the Alpine lithosphere particularly challenging.

Since Aki et al. [1977], the most basic and often used method to image seismic heterogeneities in the upper mantle is teleseismic tomography. It is based on the inversion of observed relative arrival times of P (or S) waves generated by earthquakes at teleseismic distances (>20°) for relative variations of P (or S) wave velocity (V_{p}, or V_{s}) in the upper mantle beneath a seismic array. Teleseismic tomography has been widely used to image fast-velocity slabs interpreted as subducted continental and/or oceanic lithosphere in the Alpine upper mantle [e.g., Lippitsch et al., 2003, Piromallo and Morelli, 2003, Zhao et al., 2016a, Paffrath et al., 2021]. Contrasting results of these mantle tomography studies have led to controversies about the geometry of the slabs at depth, including whether the European slab is attached or detached in the western Alps [e.g., Zhao et al., 2016a], or whether Europe is the upper or lower plate in the eastern Alps [e.g., Lippitsch et al., 2003]. These questions are still of the utmost importance to understand the past and present dynamics of the mountain belt. A major issue for teleseismic tomography is the difficulty in separating the contribution of the crust from that of the mantle in arrival times for near-vertical ray paths [e.g., Waldhauser et al., 2002]. This is of particular importance in mountain ranges such as the Alps due to strong changes in crustal thickness.

The mantle structure can also be imaged with teleseismic surface-wave tomography [e.g., El-Sharkawy et al., 2020]. Frequency-dependent traveltime data of surface waves are inverted for S-wave velocity as for ambient-noise tomography, but using periods >30 s. To overcome the poor sensitivity of such long period surface waves to crustal structure, Kästle et al.

[2018] have jointly inverted dispersion data from ambient noise correlations in the short-period band (8–30 s) with data from teleseismic surface-wave records at longer periods. The horizontal resolution of the resulting shear-wave velocity models however remains rather low in the upper mantle, limiting the value of this type of model in the debates on slab geometry beneath the Alpine range.

1.2. *Ambient noise imaging in the Alps before AlpArray*

Ambient noise tomography (ANT) is particularly well suited to imaging the Alpine crust as a complement to the methods outlined in the previous section because (a) it does not require local earthquakes [Shapiro et al., 2005], and (b) the period range of seismic noise is adequate for crustal imaging, in contrast to teleseismic surface wave tomography which is dominated by longer wavelengths. A sufficient coverage of the study region by seismic arrays is the only requirement for a fairly resolved 3-D velocity model since each station becomes a wave source for all other stations in the noise cross-correlation process [Campillo and Paul, 2003, Shapiro and Campillo, 2004].

Since the first application of ambient noise tomography to the Alps by Stehly et al. [2009], station coverage has improved significantly in density but also in spatial homogeneity. This improvement is due to numerous new permanent broadband stations (in Austria, Germany, France, etc.) and to temporary networks, most importantly the AlpArray seismic network [AASN; AlpArray Seismic Network, 2015]. Indeed the AASN, which included more than 600 stations, was designed to fill in gaps between permanent stations and to homogenize spatial coverage in a way that no location in the Alps was more than 30 km away from a seismic station onland [Hetényi et al., 2018a]. The AASN also had a marine component with 29 ocean-bottom seismometers (OBS) deployed for 8 months in the Ligurian basin. It was complemented by denser quasi-linear or 2-D temporary arrays on targets of specific interest. The most important ones were EASI across the Eastern Alps [AlpArray Seismic Network, 2014], CIFALPS and CIFALPS-2 across the Western Alps [Zhao et al., 2016b, 2018], and Swath-D in the Central and Eastern Alps [Heit et al., 2017]. Figure 1 shows the seismological stations prior to

2010, and the stations which were used in the studies summarised in this review. For seismic tomography in general, and ambient noise tomography in particular, there is clearly a time before and a time after AlpArray.

Before AlpArray, the limited coverage of large parts of the Alpine area only allowed for ambient noise tomography studies of the central Alps, relying mainly on the dense Italian and Swiss permanent networks [Stehly et al., 2009, Verbeke et al., 2012, Molinari et al., 2015]. The pioneering application of ANT to the Alps by Stehly et al. [2009] used records of 150 broadband stations in Switzerland and neighbouring countries. They applied a classical two-step procedure, with an inversion of dispersion measurements for group velocity maps of Rayleigh waves in the 5–80 s period band, followed by a non-linear Monte Carlo inversion of the dispersion curve in each cell for a 1-D shear-wave velocity model. The set of 1-D models were then merged into a so-called 3-D V_s model that should more properly be called pseudo 3-D. This study provided a data constrained Moho depth map of the Western Alps, because crustal thickness was a free parameter in the inversion. This Moho map shared many similarities with the reference map computed by Waldhauser et al. [1998] from depth-migrated controlled-source seismic data, including strong and abrupt Moho depth changes from 25–30 km beneath the European forelands and the Po plain, to 55 km beneath the internal Alpine arc from southern Switzerland to the Dora Maira massif (Piemonte, Italy). This first successful application of ANT in the Alps was considered a proof of concept. The tomography by Stehly et al. [2009] was followed by those of Verbeke et al. [2012] and Molinari et al. [2015], who expanded the station array to the Italian and Slovenian permanent broadband networks and the tomography to the Apennines, and used both group and phase velocity dispersion data.

In the last large-scale ANT before AlpArray, Kästle et al. [2018] used records of 313 permanent stations covering the broad Alpine region and the Apennines. To overcome the sparse station coverage in the external, western and northern Alps, they complemented ambient noise phase dispersion measurements with two-station measurements from regional and teleseismic earthquake records. The ambient noise and earthquake-based dispersion datasets agreed well enough in the overlapping period band 8–60 s to

be jointly inverted for Rayleigh and Love wave phase velocity maps in the broad period range 4–250 s [Kästle et al., 2016]. In a second stage, Kästle et al. [2018] jointly inverted Rayleigh and Love-wave phase dispersion data in each cell for 1-D V_p and V_s models of the crust and upper mantle. According to the authors, the 3-D V_s model of the upper mantle derived from joint inversion has much higher resolution than when each individual dataset, ambient noise and earthquake-based, is inverted alone. By averaging the crustal thickness of the 500 best-fitting V_s models, Kästle et al. [2018] computed a Moho depth map that compares remarkably well with receiver function and DSS Moho depth estimates along numerous profiles across the Alps and Apennines [Kummerow et al., 2004, Spada et al., 2013, Zhao et al., 2015].

The installation of the AlpArray temporary seismic network started in Austria in the summer of 2015 and ~200 of the planned 267 temporary stations were operating by mid-2016 [Hetényi et al., 2018a]. By adding the first months of AASN recordings (until June 2016) to a four-year noise dataset from European-wide permanent broadband networks, Lu et al. [2018] achieved the first ANT of the broad Alpine region with fairly homogeneous coverage and an average station spacing of ~50 km. This study was the first in a series of noise-based isotropic and anisotropic tomography studies on the Alpine lithosphere that have built on the spatial homogeneity and density of the AlpArray dataset (from both permanent and temporary stations) to develop and apply new data analysis and imaging methods.

Indeed, the high spatial density of AASN and associated permanent and temporary networks has driven methodological advances in ambient noise tomography, just as the USArray Transportable Array has driven the advent of Eikonal tomography [Lin et al., 2009]. The present paper focuses on key methodological advances on isotropic (Section 2) and anisotropic (Section 3) imaging. We also show how the application of these new methods to Alpine data opens new perspectives (Section 4) for the geological and geodynamic modeling of the Alpine belt.

2. Isotropic ambient noise tomography

The homogeneous coverage provided by the AASN motivated a number of ambient noise isotropic tomography studies on regional targets in and around

the Alps [e.g., Guerin et al., 2020, Molinari et al., 2020, Sadeghi-Bagherabadi et al., 2021, Schippkus et al., 2018, Szanyi et al., 2021]. In this section we focus on noise-based isotropic tomography studies of the broad Alpine region and surroundings using all or most available stations in Western Europe at the time of study. We describe three key improvements to isotropic imaging with cross correlations in this highly heterogeneous area.

2.1. *Second-order cross-correlation techniques*

The Ligurian basin, which separates the Corsica–Sardinia block from the southern coast of France and north-western Italy (Figure 1) is a back-arc basin generated by the rollback of the Adriatic slab in Oligo-Miocene time [e.g., Rollet et al., 2002]. Situated at the transition between the Alps and Apennines mountain ranges, it was considered an important target for the AlpArray temporary seismic experiment, which therefore included 24 broadband ocean-bottom seismometers (OBS, Figure 1).

Ambient noise tomography of an offshore area is possible without OBSs provided that it is surrounded by land stations. For example, Magrini et al. [2022] have computed an S-wave velocity model of the west-central Mediterranean, including the Ligurian basin, from surface-wave tomography using records of onland stations in Europe and North Africa. Lateral resolution in the Ligurian basin and its margins remains limited, due to lack of OBS data, illustrating that the integration of land and sea-based observations is a key target for noise-based imaging in coastal and offshore areas. Such land-sea data integration was the target of a specific effort for methodological development by Nouibat et al. [2022b]. This work aimed at solving the issues of ANT from OBS data, as OBSs are generally deployed for less than a year, and signal quality is lower than that of land stations. In this section, we summarize how Nouibat et al. [2022b] enhanced the signal-to-noise ratio of noise correlations between sea-bottom stations by computing second-order correlations with on-land stations as virtual sources.

At periods longer than 20 s, OBS recordings are affected by tilt and compliance noise induced by the soft seabed on which the instruments rest. Crawford et al. [1998] and Crawford and Webb [2000] have derived a specific pre-processing scheme based on the recordings of the pressure component of OBS records and comparison between horizontal and vertical velocity components. Nouibat et al. [2022a] and Nouibat et al. [2022b] applied this pre-processing to the AlpArray OBS recordings, along with corrections for instrument noise (glitches) at a few stations.

These noise reduction procedures were insufficient to ensure the emergence of clean Rayleigh waves in noise correlations for OBS station pairs, due to seafloor currents, boat traffic, marine animals and seismic waves in the water column. Since the recordings of onshore stations are free of such noise, Nouibat et al. [2022a,b] have synthesized Rayleigh waves between OBS stations by using onshore stations as virtual sources. This procedure is named C2, or iterative noise correlation because it recovers the Rayleigh-wave signal between two OBSs by correlating Rayleigh-wave signals emerging from correlations between these OBSs and onland stations. The C2 method relies on the stationary phase theorem. Onland stations used as virtual sources must be located close to the azimuth of the OBS pair to optimize constructive interference of the wavefields radiated by the source and recorded by the two OBS. In Nouibat et al. [2022a,b], virtual sources were selected in azimuths close (±20°) to the azimuth of the OBS pair. Since virtual sources are mostly distributed to the North and East of the OBS array, Nouibat et al. [2022b] enhanced the coverage by separate use of the causal and anticausal parts of the first-order correlations (C1: between OBSs and land stations) to compute the OBS–OBS second-order correlations (C2). Extensive tests show that Rayleigh wave signal quality may be higher in OBS–OBS correlations (C1) than in C2 correlations in the 5–10 s period range with lower water column noise. For each OBS–OBS pair, Nouibat et al. [2022b] selected the correlation of highest quality after checking the coherence of C1 and C2 correlations. Figure 2 documents how this procedure improves inter-OBS signal quality, and thus ray coverage inside the Ligurian basin, enabling high-resolution ambient noise tomography of the crust in the basin.

2.2. *Bayesian and transdimensional inference*

A primary objective of (isotropic) seismic tomography of the Alpine lithosphere is a depth map of the crust-mantle boundary at a resolution of a few tens
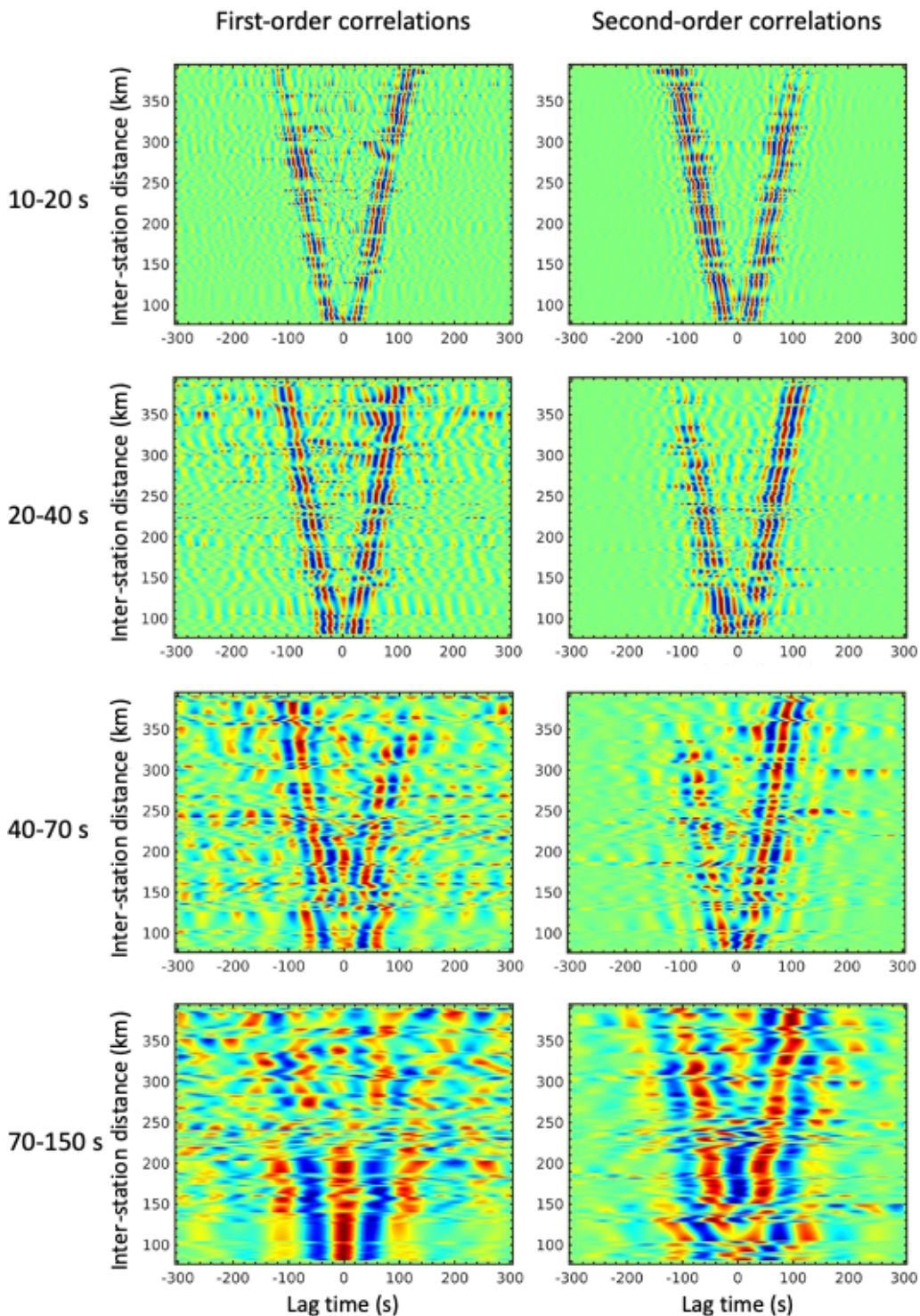
Figure 2. Inter-OBS noise correlation waveforms (Z comp.) generated in four frequency bands by: (left) first-order, standard correlation of pre-processed noise records; (right) second-order correlation using land stations as virtual sources. Modified from Nouibat et al. [2022b].

of km. More precisely, a geological [Calcagno et al., 2008] and potentially geodynamic modeling of the mountain belt requires depth maps of the superposed European, Adriatic and Ligurian Moho surfaces affected by the subduction of the Alpine Tethys, the following collision of the European and Adriatic margins, and the opening of the Ligurian backarc basin. Seismic studies prior to the AlpArray project mapped the European Moho to a maximum depth of 55 km below the belt axis [e.g., Spada et al., 2013, Stehly et al., 2009, Kästle et al., 2018]. Receiver functions of the CIFALPS transect in the south-western Alps provided the first seismic evidence for continental subduction, including converted waves on the deep European Moho at 75–80 km beneath the westernmost Po plain, and negative-polarity conversions on an "inverted" Moho between the Adriatic mantle wedge on top and the European crust below, as shown in Figure 3b [Zhao et al., 2015, Paul et al., 2022].

To take full advantage of the increased station density and to avoid dependence on arbitrary choices such as an initial model, several improvements were made to the inversions for V_s with depth.

2.2.1. *1-D depth inversion for V_s with a full exploration of the model space*

A first improvement of the 1-D inversion for V_s was performed by Lu et al. [2018], who used a subset of AlpArray data, as station installation was still ongoing. Their inversion for group velocity maps involved a linearized inversion method based on ray theory [Boschi and Dziewonski, 1999], and an adaptive parameterization scheme that reduced cell size in areas with high path density.

In the 1-D inversion stage for V_s, they built upon the inversion method of Macquet et al. [2014], where a full exploration of the model space was combined with a linear inversion for V_s. In this way, Lu et al. [2018]'s inversion for V_s included two steps. The first one used a grid search approach to uniformly sample and calculate group velocity dispersion curves for a low-dimensional model space based on a three-layer crust above a mantle half-space. This full model exploration was feasible because the dispersion curves can be computed with normal mode summation, and is computationally tractable. It was thus possible to determine an ensemble of models for which the dispersion curve matched the observed one. This

first inversion step provided for each geographical grid cell a probabilistic V_s model and the probability to have a layer boundary at a given depth. However, to reduce the size of the model space to explore, the parameterization did not allow for low velocity zones. The second step was a linear inversion for V_s, where the problem was linearized around the mean of the probability distribution obtained at the previous step.

The dense station coverage and the two-step 1-D inversion scheme for V_s combining probabilistic sampling and linear inversion resulted in a (pseudo) 3-D V_s model with significantly higher spatial resolution than, for example, the model by Kästle et al. [2018]. Comparison with controlled-source reflection profiles [ECORS-CROP: Sénéchal and Thouvenot, 1991; TRANSALP: Kummerow et al., 2004] and receiver function stacked sections across the Alpine belt [TRANSALP: Kummerow et al., 2004; CIFALPS: Zhao et al., 2015, Paul et al., 2022] displayed striking coincidence in Moho depth despite the poor sensitivity of surface-wave dispersion to layer boundaries (see Figures 3b,c for the CIFALPS transect). Lu et al. [2018] computed three depth maps of Moho proxies in the Alpine region using the probability of interface occurrence, the depth gradient of V_s and the isovelocity surface $V_s = 4.2$ km/s. These maps revealed new features such as an 8-km abrupt Moho step beneath the external crystalline massifs of the Western Alps, from Pelvoux to Mont-Blanc, which had not been detected by the ECORS-CROP DSS profile presumably due to poor signal penetration.

The 3-D V_s model by Lu et al. [2018] however failed to clearly image the continental subduction of Europe beneath Adria in the western Alps, which had been identified by receiver functions (Figures 3b,c). Since the inversion of Lu et al. [2018] was based on a simplified parameterization (only three crustal layers), and on a final optimization framework, the solution was a unique model that explains observations, but without associated uncertainties and trade-offs. In this way, this unique solution did not depict the full state of information contained in the data.

2.2.2. *1-D depth inversion for V_s with transdimensional inference*

The next step in methodological improvement was therefore to carry out inversions within a full
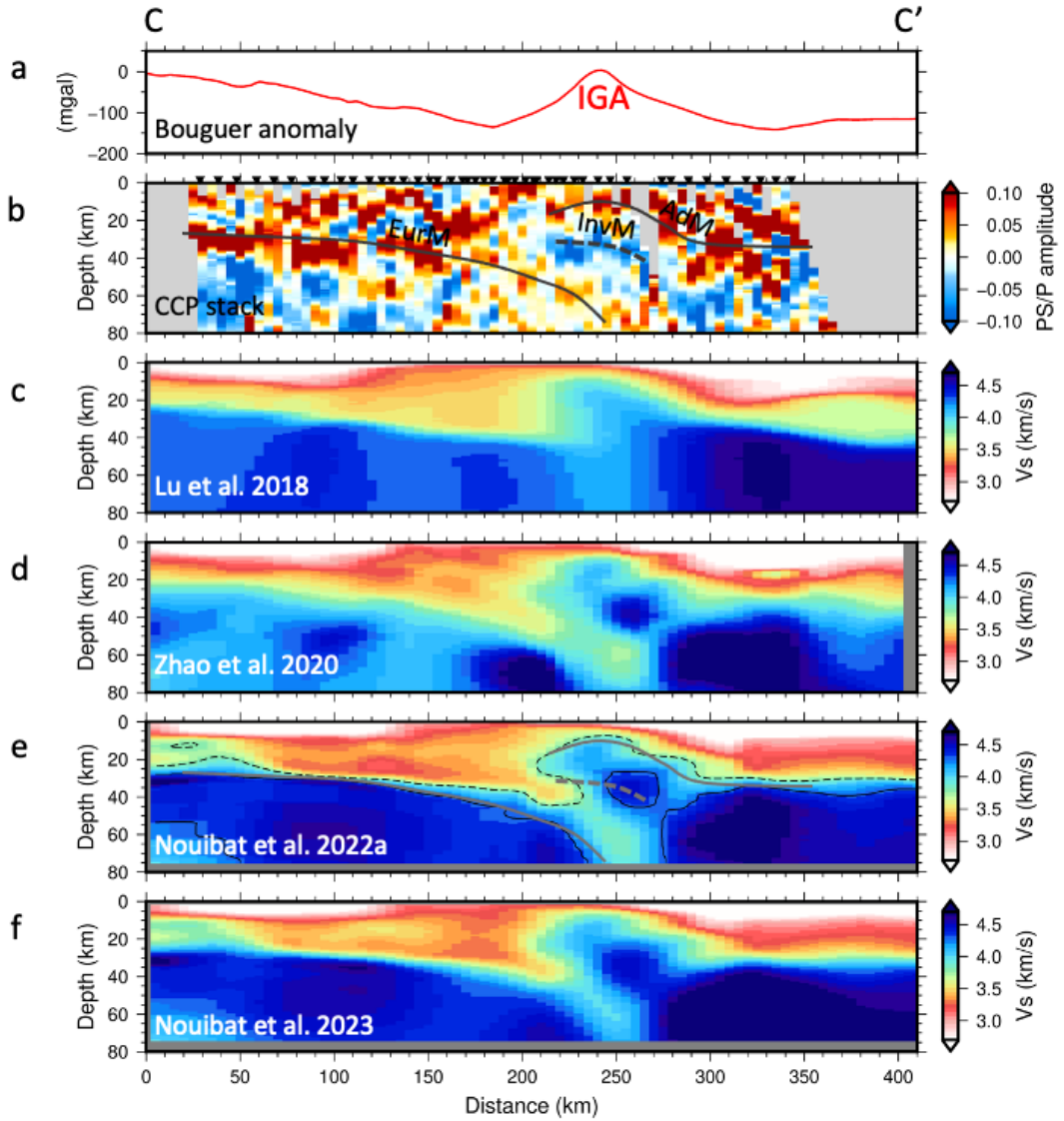
Figure 3. Cross-sections along the CIFALPS profile in the southwestern Alps (CC′, location shown in Figure 1b). (a) Bouguer anomaly from Zahorec et al. [2021]; IGA: Ivrea gravity anomaly. (b) Common-conversion point (CCP) stack of receiver functions at stations of the CIFALPS experiment; locations of stations projected onto the CIFALPS profile are shown as black inverted triangles at the surface; the solid thick black lines are the European Moho (EurM) and the Adriatic Moho (AdM) that appear as converted waves of positive amplitude (in orange-red); the dotted thick black line shows an inverted Moho (InvM, higher velocity on top than on the bottom), which is marked by converted waves of negative amplitude (in blue); modified from Paul et al. [2022]. (c) Shear-wave velocity model from the ambient noise tomography of Lu et al. [2018]. (d) Shear-wave velocity model from the ANT with transdimensional inversion to V_s by Zhao et al. [2020]. (e) Shear-wave velocity model from the ambient noise tomography of Nouibat et al. [2022a]; dashed black line: V_s = 3.8 km/s velocity contour; continuous black line: V_s = 4.3 km/s velocity contour (Moho proxy); the thick grey lines are the Moho boundaries shown as black lines in (b). (f) Shear-wave velocity model from the ambient noise wave-equation tomography of Nouibat et al. [2023].

Bayesian framework and a fully adaptive parameterization, without any linearization, and where the solution is a full probability distribution, therefore providing uncertainty estimates. In this context, Zhao et al. [2020] performed a Bayesian transdimensional inversion of the group-velocity Rayleigh-wave dispersion data of Lu et al. [2018] with a focus on the western Alps (4.5°E–9°E; 44°N–46.7°N). Unlike the inversion by Lu et al. [2018], which assumed a four-layer model, the transdimensional inversion treats the number of layers as an unknown parameter [Bodin et al., 2012, Yuan and Bodin, 2018]. At each gridpoint, Zhao et al. [2020] inverted dispersion data for V_s perturbations around a homogeneous half-space reference model with velocity 3.8 km/s, allowing a wide range of velocity variations (±50%).

The resulting (pseudo) 3-D V_s model (Figure 3d) displays a channel of anomalously low shear-wave velocities (V_s = 3.6 km/s) at 70-km depth beneath the fast-velocity, high-density Ivrea body anomaly in the CIFALPS cross-section (IGA in Figure 3a). This low-velocity anomaly is located between the deep European Moho and the inverted Moho of the Ivrea body imaged by receiver functions of the CIFALPS experiment (Figure 3b). The transdimensional inversion of Zhao et al. [2020] was thus able to image the subduction of the European continental lithosphere beneath the Adriatic lithosphere with minimal a priori constraints.

2.2.3. *3-D tomography with transdimensional inversions*

The third methodological improvement carried out by Nouibat et al. [2022a] was to use the entire AASN dataset and apply a full transdimensional approach at both stages of the inversion, that is in the 2-D inversions for group velocity maps and in the 1-D inversions for V_s. At each period, a transdimensional inversion was carried out to obtain probabilistic Rayleigh-wave group-velocity maps following Bodin et al. [2012]. In the second stage, a full transdimensional approach was used to invert for V_s at each geographical location the dispersion curve obtained in the first stage.

The key benefit of the transdimensional inversion for group velocity maps is that spatial parameterization is treated as part of the inversion, allowing local resolution to adapt to data density. Another improvement introduced by Nouibat et al. [2022a] is the computation of uncertainties on group velocity estimates by transdimensional inversion; these uncertainties are then incorporated into the inversion for V_s (second stage). Young et al. [2013] and Pilia et al. [2015] were the first studies to use this two-step transdimensional procedure, with uncertainty computed in the first stage used to weight the input in the second.

In the first stage, to account for the strong lateral velocity contrasts of the Alpine crust, straight rays of the classical forward model were replaced by bent rays with the ray geometry updated at each iteration using the fast marching method of Rawlinson and Sambridge [2004]. Nouibat et al. [2022a] applied this new inversion scheme to four years of noise records from ~1440 permanent and temporary seismic stations, including the entire AlpArray network with its offshore component (Z3 network: AlpArray Seismic Network 2015), the two CIFALPS experiments [YP and XT networks: Zhao et al., 2016b, 2018], and the EASI experiment [XT network: AlpArray Seismic Network, 2014] (Figure 1). Data coverage is improved compared to Lu et al. [2018], and so to Zhao et al. [2020], especially in the Western Alps and the Ligurian Basin.

Figure 3e shows a depth section along the CIFALPS transect in the 3-D V_s model by Nouibat et al. [2022a], which may be compared to the models by Lu et al. [2018] shown in Figure 3c, and Zhao et al. [2020] shown in Figure 3d. Unlike Lu et al. [2018] and similar to Zhao et al. [2020], Nouibat et al. [2022a] image the dipping low-velocity layer beneath the Ivrea body high-density, high-velocity anomaly (IGA, x = 210–300 km in Figure 3), which is indicative of the continental subduction of Europe beneath Adria. As the Zhao et al. [2020] inversion for V_s was based on the same dispersion dataset as Lu et al. [2018], and as Nouibat et al. [2022a] used the same inversion method for V_s as Lu et al. [2018], but with a different set of four-layer models, we propose that the major difference between Figures 3c and 3e is related to the difference between the sets of velocity models explored in the probabilistic inversion for V_s: 130 million for Nouibat et al. [2022a], and 8 million for Lu et al. [2018]. In particular, the complex vertical velocity profiles of the subduction region with alternating high and low velocities were not explored by Lu et al. [2018]. Vertical velocity gradients are stronger in Nouibat et al. [2022a]'s model (Figure 3e) than in Zhao et al. [2020]'s model (Figure 3d), in particular at the crust-mantle boundary. Even

though the input data and the inversion schemes differ, the overall similarities between the two models of Figures 3e and 3f suggest that the differences in velocity gradient at the Moho may result from the parameterization of the inversions for V_s. While the probabilistic inversion of Nouibat et al. [2022a] assumes a four-layer starting model with a velocity jump at Moho, the reference velocity model in the transdimensional inversion of Zhao et al. [2020] is a homogeneous half-space with no discontinuity. This a priori uniform distribution of velocity may favor a smooth velocity gradient at the Moho. The V_s model by Nouibat et al. [2022a] with its a priori imposed sharp crust-to-mantle velocity contrast is more in line with previous controlled-source (ECORS-CROP in the north-western Alps) and receiver function profiles [CIFALPS: Figure 3b; CIFALPS-2, Paul et al., 2022], which display clear reflected and converted phases on the Moho. The impact of other refinements in the Nouibat et al. [2022a] inversion methodology (error estimates on group velocities, bent rays) is difficult to evaluate due to the differences in the input data coverage. It would be an interesting test to apply the fully transdimensional inversion for V_s of Zhao et al. [2020], with an a priori constraint on the velocity jump at the Moho, to the group velocity data with uncertainties of Nouibat et al. [2022a].

2.3. *Wave-equation tomography*

To compute shear-wave velocity models of the crust and uppermost mantle from Rayleigh-wave traveltime data between station pairs, Lu et al. [2018] and Nouibat et al. [2022a] have used a two-stage inversion scheme, which, in spite of improvements related to a probabilistic approach, is a standard strategy for ANT. The first stage, a series of 2-D inversions of traveltime data for group velocity maps at selected periods, is based on ray theory, which is only valid at infinite frequency. The second stage, a set of 1-D inversions of the local dispersion curves for S-wave velocity, results in 1-D models merged into a pseudo 3-D model. The strong crustal heterogeneity of the Alps and surrounding areas, including the Ligurian back-arc basin, makes the ray hypothesis particularly inadequate. This area therefore provides an excellent chance of testing a tomography procedure that better accounts for the physics of seismic wave propagation. In this section, we first describe a new

wave-equation based approach of ambient noise tomography called wave equation tomography [WET, Lu et al., 2020] for the elastic case, using only land station recordings. We next present the extension of the WET method to include elastic–acoustic coupling at the sea bottom and OBS records [Nouibat et al., 2023].

2.3.1. *Wave-equation onshore tomography (elastic case)*

To calculate a truly three-dimensional V_s model consistent with wave propagation physics, Lu et al. [2020] derived a wave-equation based approach, hence called ambient noise wave-equation tomography. As in the ambient noise adjoint tomography of Chen et al. [2014], the observable is travel time (i.e. phase) of the Rayleigh wave reconstructed from noise correlation, while full-waveform inversion (FWI) would invert amplitude and time. Indeed, Rayleigh wave amplitudes are not correctly retrieved by the classical noise correlation procedure [e.g., Campillo, 2006]. FWI of ambient noise correlation signals probably has great potential for lithospheric imaging. It is not yet operational because it would require specific pre-processing of noise records for a better retrieval of amplitudes and, more importantly, an accurate estimate of noise source distributions and emitted waveforms [e.g., Fichtner, 2014, Sager et al., 2018].

The wave-equation tomography (WET) approach implemented by Lu et al. [2020] consists of iteratively updating an initial ambient noise tomography model (from the two-stage traditional method) by minimising frequency-dependent phase traveltime differences between the Rayleigh waveforms observed in noise correlations and the synthetic waveforms computed by 3-D numerical modeling of wave propagation. Synthetic waveforms are computed with the 3-D elastic wave equation solver of the SEM46 package [Trinh et al., 2019] based on the spectral element method [Komatitsch and Vilotte, 1998, Komatitsch and Tromp, 1999]. Of the 304 stations located in the study region, a subset of 64 suitably located stations were selected as virtual sources by Lu et al. [2020], and the signal bandwidth was limited to [10–50 s] to ensure acceptable computing time. The observed signal for a station pair is the Rayleigh wave part of the Green's function, estimated from the time derivative of the cross-correlation of seismic noise.

The synthetic signal is the convolution product of a bandpass filtered Dirac delta source function with the synthetic Green's function computed with SEM46 for a source–receiver pair, and a vertical force applied on the free surface at the source location. The misfit function is then computed from the frequency-dependent phase traveltime differences between observed and synthetic waveforms. The adjoint-state approach is used to compute the misfit gradients [e.g., Tromp et al., 2005], and the inversion is conducted as an iterative local optimization problem.

The final S-wave velocity model obtained by Lu et al. [2020] after 15 iterations of wave equation tomography has a 65% lower total misfit than the initial ANT model by Lu et al. [2018]. This strong misfit reduction is mostly due to periods larger than 25 s, where the WET has corrected for a strong and unexplained positive shift of the traveltime misfit histograms in the initial model. A direct consequence is that the final V_s model has significantly higher average velocities at lower crustal depth (30 km). Beyond this tuning of average velocities, the WET approach was able to retrieve finer scale heterogeneities than the ANT model, for example a high-velocity anomaly at 10 km depth, which is closer in shape to the well-known Ivrea positive Bouguer anomaly [see Figure 8 in Lu et al., 2020].

2.3.2. *Wave-equation onshore/offshore tomography (with acoustic–elastic coupling)*

As compared to Lu et al. [2018], a more accurate ANT model of the Alpine region and its surroundings was computed by Nouibat et al. [2022a] using a larger noise correlation dataset including recordings of sea-bottom seismometers in the Ligurian basin, and an improved inversion scheme (see Section 2.2). Like Lu et al. [2020], Nouibat et al. [2023] have performed a WET to improve the model of Nouibat et al. [2022a] by accounting for three-dimensional and finite-frequency effects of wave propagation. A major improvement achieved by Nouibat et al. [2023] is the inclusion of the water layer effect on wave propagation in the Ligurian basin. The vertical-component record of short-period (<20 s) surface waves at ocean-bottom stations is dominated by a fluid–solid interface wave named Rayleigh–Scholte wave that propagates at lower speed than the Rayleigh wave in the elastic medium. At periods

>20 s, the effect of the water layer becomes negligible for the Ligurian basin (max. water depth 3 km) because the Rayleigh wavelength is large compared to water depth [Nouibat et al., 2023]. Accounting for the effect of the water layer in the forward simulation of surface-wave propagation and in the inversion of traveltime observations for shear-wave velocity is therefore required to enhance resolution in the shallow layers of the Ligurian basin.

For their wave-equation tomography with elastic–acoustic coupling, Nouibat et al. [2023] selected, from the dataset of Nouibat et al. [2022a], 600 stations as receivers, out of which 185 were selected as sources based on noise correlation signal quality. The initial model was the ANT V_s model computed by Nouibat et al. [2022a]. As in Lu et al. [2020], the inverse problem minimised the frequency-dependent phase traveltime differences between observed and synthetic vertical-component waveforms for considered source–receiver pairs. The inversion was conducted in the 5–85 s period range, considering elastic–acoustic coupling in the forward simulation in the 5–20 s band. Unlike Lu et al. [2020], the velocity model was updated progressively from long periods (40–85 s) to shorter ones, 20–40 s, 10–20 s then 5–10 s to avoid cycle skipping.

The final WET V_s model differs significantly from the initial ANT V_s model, particularly in shallow layers of the Ligurian Basin, and in the most heterogeneous parts of the Alpine crust. These discrepancies highlight the importance of accounting for the physics of wave propagation, i.e. elastic–acoustic coupling at the sea-bottom, finite-frequency effects and 3-D propagation. In the alpine crust (i.e. onland), velocity contrasts tend to be slightly enhanced, in particular at lower crustal depth [26 km, see Figure 6 in Nouibat et al. [2023]], while the location and shape of velocity changes are preserved with respect to the initial ANT model (Figures 3e–f). At depths shallower than ~10 km, S-wave velocities in the Ligurian basin are ~8% lower in the WET model than in the ANT model, in agreement with the lower velocities of the Rayleigh–Scholte wave. Accounting for the water layer in the Ligurian basin also leads to higher velocities in the crust of western (Variscan) Corsica.

Nouibat et al. [2023] conducted extensive evaluation of the robustness of their WET model. The quality of the S-wave velocity model was documented

by traveltime misfit maps at representative periods between 8 and 55 s. As expected, misfit is lower for the WET model than for the initial ANT model, except in the peripheral poorly illuminated regions [see Figure 12 in Nouibat et al., 2023]. The footprint of the broad geological structure has disappeared, whereas it was clearly visible for the ANT model at periods ≥20 s. Using the weak sensitivity of Rayleigh wave phase velocity to V_p, Nouibat et al. [2023] also inverted Rayleigh wave dispersion observations for P-wave velocity, starting from an initial V_p model computed from the initial (ANT) V_s model using an empirical formula. To document the robustness of their P and S-wave models, they computed synthetic waveforms for a regional earthquake in Switzerland and compared to observed waveforms in three frequency bands between 2 and 10 s. The fit between simulated and observed seismograms is striking for the travel times of the P and Rayleigh waves, but also for relative amplitudes between the wave trains. Such a high coherence in the short-period bands is a reliable indication that wave equation tomography is capable of imaging small-scale crustal structures. This synthetic test also demonstrates that the WET V_s and V_p models derived from ambient noise correlations would be a good initial model for a wave-equation tomography using earthquake records. As regional earthquake records include both body and surface waves, the resulting P-wave velocity model would be much more accurate than that obtained from Rayleigh wave travel time inversion alone, due to its weak sensitivity to V_p.

2.4. *Model validation: Moho depth*

Surface waves are weakly sensitive to velocity contrasts, but Bayesian inversions for V_s were shown to be very effective for imaging the crust-mantle boundary [Lu et al., 2018, Nouibat et al., 2022a]. Comparisons of Moho depths imaged by other geophysical methods such as DSS profiles (ECORS-CROP) and receiver function analyses have shown that selected iso-velocity surfaces in the ambient noise derived 3-D V_s models are reliable proxies of the Moho [Nouibat et al., 2022a, Paul et al., 2022, Nouibat et al., 2023]. For example, the velocity contour $V_s = 4.3$ km/s is a good proxy for the European Moho, and the Adriatic Moho outside the Ivrea body region, as shown by the coincidence of this surface with Moho conversions picked from CCP receiver function stacks along the CIFALPS and CIFALPS2 sections (see for example Figure 3e). In the Ivrea body region, the Moho imaged by the ECORS-CROP DSS profile and receiver function sections is better approximated by the 3.8 km/s velocity surface, probably because the external rim of the Ivrea body is made of serpentinized peridotites with lower velocities than dry peridotites [Figure 3e; see discussion in Malusà et al., 2021]. In the Ligurian basin, a comparison of the V_s model of Nouibat et al. [2022a] with a V_p model derived by Dannowski et al. [2020] from refraction and wide-angle reflection OBS data shows a striking coincidence of the V_p Moho (iso-velocity 7.2 km/s) with the 4.1 km/s V_s contour [see Figure 9 in Nouibat et al., 2022b]. A Moho depth map of much higher resolution than previous ones [e.g., Grad et al., 2009, Spada et al., 2013] can therefore be built by mapping iso-velocity contours of the V_s models by Nouibat et al. [2022a] and Nouibat et al. [2023].

3. Anisotropic ambient noise tomography

Surface waves in seismic noise correlations can potentially shed new light on anisotropy in the Earth's crust and upper mantle, overcoming the observational biases related to the uneven distribution of earthquakes, which leads to uneven azimuthal coverage [for a review, see Maupin and Park, 2015].

Our knowledge of azimuthal anisotropy beneath the Alps and Italy mostly comes from XKS splitting studies. Fast velocity directions are generally parallel to the mountain chain in the Western and Central Alps [Barruol et al., 2004, 2011, Lucente et al., 2006, Salimbeni et al., 2018], the Eastern Alps [Bokelmann et al., 2013, Qorbani et al., 2015] and the Apennines [Palano, 2015]. Teleseismic P wave travel time delays were used by Rappisi et al. [2022] to study anisotropy in the Central Mediterranean area, including the Alps. Both XKS and teleseismic P waves have too steep incidence angles to reliably constrain anisotropy in the crust, also because the cumulated travel time in the crust is much smaller than in the upper mantle. Studies using regional refracted Pn and Sn phases like Díaz et al. [2013] provide information about the uppermost mantle, as these waves are tied to the Moho interface and propagate with mantle velocities.

Long wavelength anisotropic structure beneath Europe is mostly known from large scale or global surface wave studies where the crust is not resolved [e.g., Kustowski et al., 2008, Weidle and Maupin, 2008, Boschi et al., 2009, Zhu et al., 2015, Nita et al., 2016, Schivardi and Morelli, 2011]. All these studies are constructed from long period observations, where the crust is not inverted for but set from a reference model such as LITHO1.0 [Pasyanos et al., 2014]. A few studies focussing on crustal anisotropy used surface waves from seismic noise correlations to characterise anisotropy at regional scale, such as Switzerland [Fry et al., 2010], the Vienna Basin [Schippkus et al., 2020], the Bohemian Massif [Kvapil et al., 2021], or the Eastern Alps [Kästle et al., 2024].

The dense station coverage (Figure 1) across the greater Alpine region during the AlpArray project provided a unique opportunity to further develop and understand the limitations of noise-based imaging methods aimed at characterising seismic anisotropy across a strongly heterogeneous structure. Since the Alpine region is heterogeneous at all scales, it is in particular crucial to reliably estimate uncertainties and identify locations and periods where systematic errors may affect azimuthal anisotropy measurements. These questions are the focus of Section 3.1.

Once uncertainties associated with surface wave velocities are estimated, they can be used in inversions for depth variations of anisotropic parameters. Reliable uncertainties are also crucial in the case of joint inversions, where different datasets are inverted simultaneously (e.g., earthquake based and noise-based observations). A Bayesian inversion framework in theory handles this question in a both intuitive and simple way, producing families of acceptable Earth models, over which it is possible to make posterior statistics. This ensemble solution can be exploited to give reliable and useful information on the Earth structure. Section 3.2 is dedicated to such strategies for both radial and azimuthal anisotropy.

3.1. *Improving observations of azimuthal anisotropy*

The effect of isotropic heterogeneities on the wavefield can map into anisotropic parameters. In this section, we give some insights into such effects

through the now well-established Eikonal tomography method [Lin et al., 2009]. We present outcomes of Eikonal tomography across the Alps and show how beamforming can improve seismic noise-based observations of anisotropy. Both Eikonal tomography and beamforming naturally correct for deviations from great circle [e.g., Pedersen et al., 2015] and uneven distribution of noise sources [e.g., Froment et al., 2010, Harmon et al., 2010], so the only main bias to handle is the one from isotropic heterogeneities.

3.1.1. *Biases in measurements of azimuthal anisotropy: insights from Eikonal tomography*

Eikonal tomography makes use of dense station networks to reconstruct the wavefield propagating away from a source [Lin et al., 2009]. In ambient noise applications, any seismic station can act as a virtual source and the signals recorded at all other stations allow us to image the wavefield. When computing ambient noise correlations, amplitudes are lost due to filters such as spectral whitening. Only the travel-time field is recovered, therefore hindering the use of amplitudes to correct for bias from wave interference.

In Eikonal tomography [Lin et al., 2009], travel times recorded at receivers are interpolated onto a regular grid. The gradient of the travel-time field then gives the phase velocity and the propagation direction at each grid point. This highlights important strengths of Eikonal tomography: it is simple to calculate and the direction of the incoming wave is directly determined from the data. In order to get the full, azimuthal anisotropic phase velocity map, the process has to be repeated for all available virtual sources so that a set of phase velocity measurements and their propagation azimuths is obtained for each grid cell. The final phase-velocity field is obtained by averaging the measured phase velocities for all virtual sources. Different statistics of the estimated phase velocities (mean, median, mode and standard deviation) can be used as uncertainty estimates. Similarly, for the anisotropic part, the residual from the fitted function provides information on the reliability of parameter estimates.

Isotropic bias can be approximately modelled by a 360° variation of phase velocity with azimuth [Lin and Ritzwoller, 2011, Mauerberger et al., 2021]. We

refer to phase velocity variations with azimuth in the following form (applicable to weakly anisotropic media):

$$C(\phi) = C_0 \big(1 + A_1 \cos(\phi - \theta_1) + A_2 \cos(2(\phi - \theta_2)) + A_4 \cos(4(\phi - \theta_4)) \big),$$ (1)

where $C(\phi)$ is the anisotropic phase velocity, dependent on the wave propagation azimuth ϕ. It is given by its isotropic component C_0 plus three anisotropy terms that describe the θ_1 anisotropy (360° symmetry), the θ_2 anisotropy (180° symmetry) and the θ_4 anisotropy (90° symmetry), where θ is the fast axis direction and A the fast axis amplitude in fractions of C_0 from zero to peak. The θ_2 anisotropy is the dominant component for Rayleigh anisotropy [e.g., Montagner and Nataf, 1986] while the non-physical θ_1 anisotropy can be used to check for potential measurement bias created by isotropic heterogeneities. The θ_4 component is not included in further discussions since it is mostly relevant for Love waves which are not taken into account in the methods described below.

Figure 4 shows systematic errors resulting from isotropic heterogeneities through synthetic data computed in a laterally heterogeneous model, onto which we apply Eikonal tomography. In Figure 4d (perfect sampling), we observe an undulating pattern in the isotropic velocities, which depends on the signal wavelength. This undulating pattern is due to the interference of waves that are refracted by the isotropic anomaly. Most of the bias, however, cancels out when averaging over sources from many directions (Figure 4e). This error can also be corrected when taking the amplitude information into account [e.g., Helmholtz tomography, Lin and Ritzwoller, 2011]. A more severe bias stems from under-sampling the wavefield (Figure 4b). To work properly, the Eikonal method requires approximately plane wavefront between adjacent receivers. If the medium is highly heterogeneous, this assumption is violated and only a smoothed version of the true wavefield can be reconstructed from the measurements at the receiver locations. The resulting error in the isotropic part mostly cancels out when signals from different azimuths are averaged (Figure 4c). In the anisotropic part, however, a systematic, azimuth-dependent error remains, resulting in spurious anisotropy around the edges of strong velocity heterogeneities.

The level of these spurious anisotropic measurements depends not only on the absolute velocity variation but also on the wavelength of the signal, the inter-station spacing and the velocity gradient at the edges of the anomalies. The controlling factor for the bias is the level of complexity of the wavefront between adjacent stations.

3.1.2. *Eikonal tomography in the Alps*

Kästle et al. [2022] presented an application of Eikonal tomography to the Alpine area, including data from the AlpArray network. They were able to resolve both the isotropic and the anisotropic parts at periods sensitive to different depth ranges from the shallow crust to the uppermost mantle. The three anisotropic components were obtained by taking the azimuthally dependent phase-velocity measurements and fitting them to Equation (1).

Kästle et al. [2022] tested for different observables that can be related to a bias in anisotropy measurements, such as the amplitude of the θ_1 component or the standard deviation from fitting the θ_2 anisotropy. They found that none of these observations are adequate to reliably identify biased measurements. More sophisticated approaches such as forward modelling the travel-time field from the isotropic velocities may be necessary. This could also be used iteratively to improve the accuracy of the interpolation for highly complex travel-time fields, at the cost of giving up the relative simplicity of the Eikonal approach. However, Kästle et al. [2022] inferred from synthetic tests that isotropic anomalies of up to 10% produce bias, which in most cases is smaller than what is identified as "true" anisotropy.

The θ_2 anisotropic component obtained by Kästle et al. [2022] is presented in Figure 5. The fast axis directions generally follow the curvature of the Alpine arc at 15 s period, representative of the upper crust. At 40 s period, the fast axis becomes more oblique to orogen-perpendicular within the central Alps. The eastern part of the Alps has more homogeneously E–W oriented fast axes from short to long period measurements. In most of the northern Alpine foreland, the anisotropic fast axis orientations are consistently following the Alpine curvature at periods between 10 and 50 s.

The uncertainties in the anisotropic measurements are largest at model boundaries, where the azimuthal coverage is non-optimal, as well as within
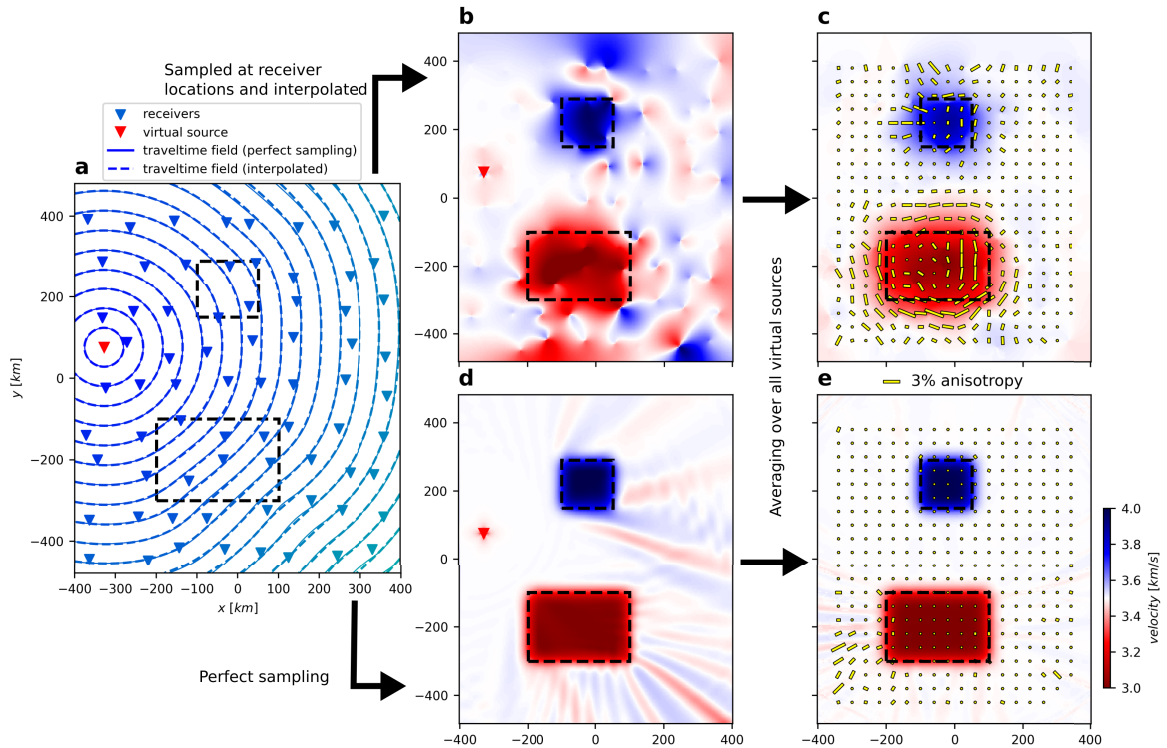
Figure 4. Example illustrating the bias in the anisotropic Eikonal tomography method. (a) 2-D wavefield propagating away from the virtual source station; black dashed lines indicate the locations of isotropic high and low velocity anomalies. (b) Isotropic phase velocities recovered by applying the Eikonal tomography method to the wavefield recorded at the receiver locations; anomalies outside the dashed lines are mainly caused by incomplete reconstruction of the true traveltime field. (d) Same as (b) for a perfectly sampled traveltime field; the striped velocity heterogeneities behind the anomalies are caused by wavelength-dependent wave interference effects. (c) and (e) Final models resulting from averaging the models for all virtual sources, i.e., swapping the position of the virtual source with all available receiver positions. The apparent anisotropy (yellow bars) is caused by velocity errors illustrated in (b) and (d) since the input model is purely isotropic.

and around the large sedimentary Po and Molasse basins north and south of the Alps. In the former, isotropic velocities indicate that velocities can be as low as −30% compared to the average velocity [Kästle et al., 2022]. These regions are therefore prone to the systematic bias mentioned above, particularly at short periods. In most of the other regions and at longer periods, the anomaly strength is usually within ±10% with smoothly varying isotropic velocities. Correspondingly, Kästle et al. [2022] found that the imaged pattern of anisotropies in the Alps is compatible with previous, more localised studies Fry et al. [2010], but also with the results from beamforming [Soergel et al., 2023; Section 3.1.3].

3.1.3. *Beamforming*

An alternative approach to Eikonal tomography is to use the phase information in a beamforming approach. Beamforming consists of, for a set of closely located seismic stations and at a given frequency, inferring the direction and local phase velocity of the incoming wave [for a review, see Rost and Thomas, 2002]]. Contrary to Eikonal tomography, the full waveform of the empirical Green function is used, as illustrated in Figure 6. The original waveforms (Figure 6a) are shifted in time using a grid search across many phase velocities and incoming directions. The final estimated phase velocity is the one
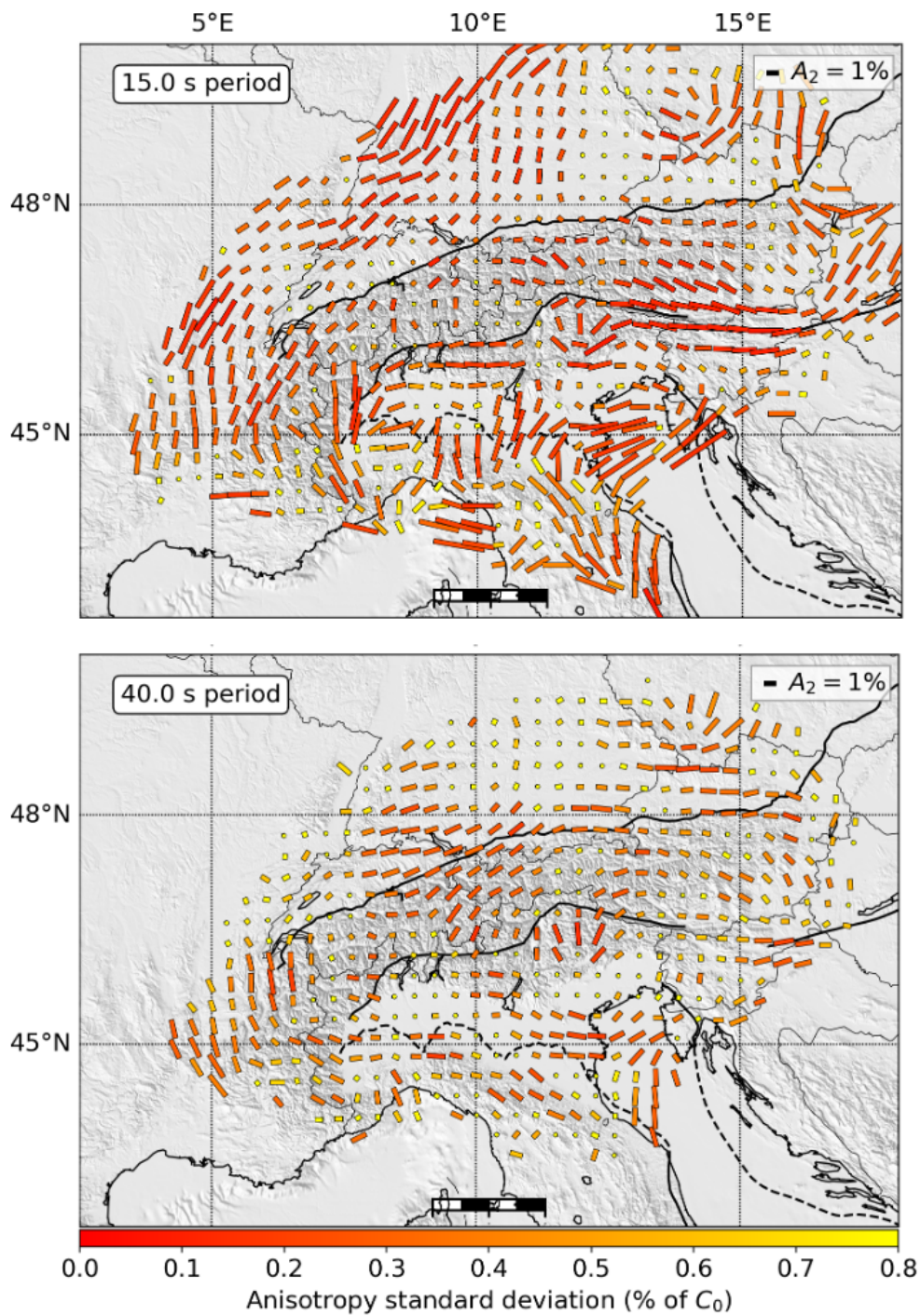
Figure 5. Maps of θ_2 azimuthal anisotropy at 15 and 40 s period resulting from Eikonal tomography in the Alps. The direction of each line shows the fast direction, and the length shows the amplitude (zero to peak). The colour of the lines gives the estimated uncertainty on the amplitude A_2 (in percent of C_0).
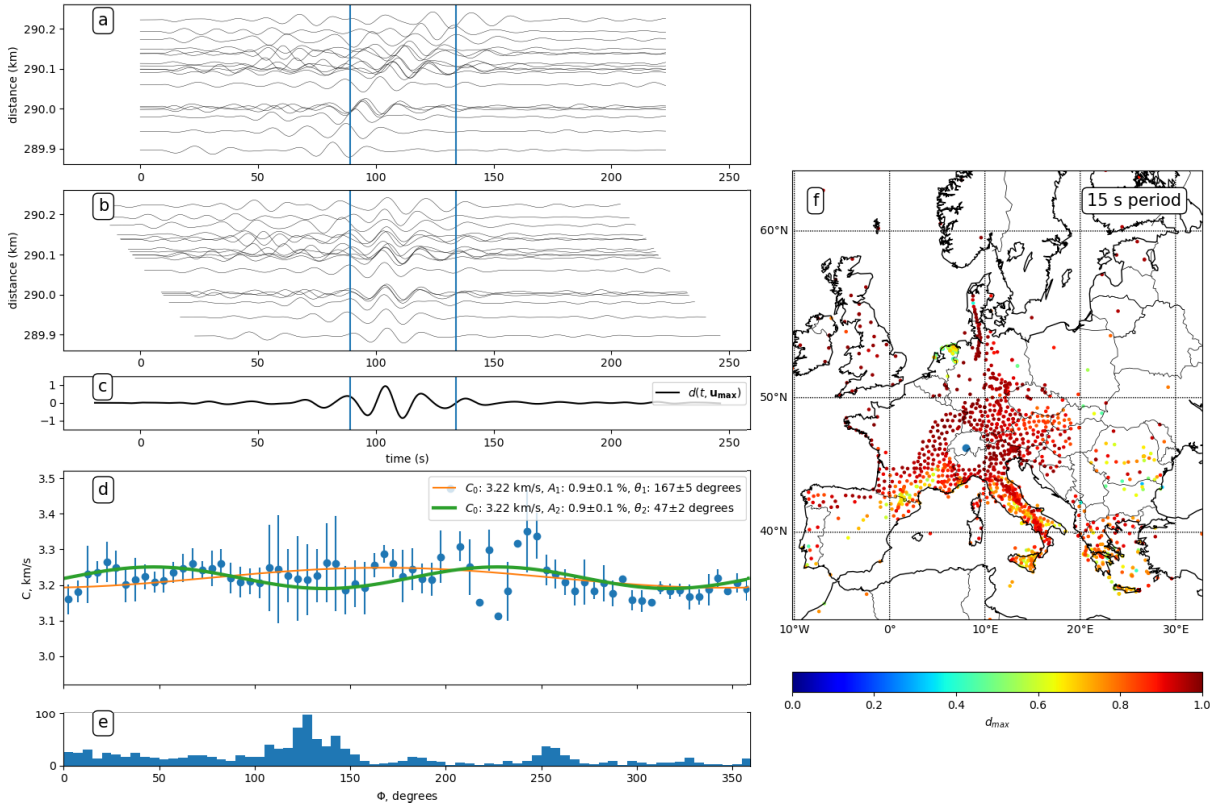
Figure 6. Illustration of data processing, and map of estimated azimuthal anisotropy at 15 s period for one seismic array. (a) Filtered traces before aligning. (b) Same traces as (a), aligned using the combination of azimuth and phase velocity for which the stack is optimal (maximum peak amplitude). (c) Stack at optimal parameters, normalised by the number of stations. The maximum of this stack is called d_{max}. (d) Phase velocity as a function of azimuth, using all source stations. The orange and green curves correspond to the first two cosine terms of Equation (1). (e) Number of source stations (binned in 5° azimuth bins) as a function of azimuth. (f) Quality of stack d_{max} for all source stations. The seismic array is centered at the blue dot. It is surrounded by a blank area, because of the need to respect a minimum distance between source and receiver stations. The colour code shows d_{max}, the maximum amplitude of the stack divided by the number of traces. Soergel et al. [2023] particularly focused on quality control and error estimates to be able to carry out inversions for anisotropic parameters with depth. Such quality control and error estimates are key input for subsequent transdimensional Bayesian inversion described in Section 3.2.

for which the traces are optimally aligned (Figure 6b), and for which the stack yields the highest maximum amplitude (Figure 6c).

Beamforming has been extensively used on seismic noise, in particular to characterise the noise field and infer the locations of origin of noise sources [for Europe, see for example Friedrich et al., 1998, Landès et al., 2010 or Juretzek and Hadziioannou,

2016]. Beamforming has also been used to quantify anisotropy on earthquake data [e.g., Pedersen et al., 2006, Alvizuri and Tanimoto, 2011] or directly on raw noise records [e.g., Riahi and Saenger, 2014].

To estimate surface wave azimuthal anisotropy, beamforming has to be carried out, for each source, across the range of target periods (Figure 6d).

This method was previously used on earthquake

data. Applying it to noise correlation is straight-forward as seismic stations can be used as virtual sources. Here we present key elements of the implementation of Soergel et al. [2023] and the application to the Alps. A somewhat similar approach was taken at the same time by Wu et al. [2023] for the Northeastern Tibetan Plateau.

The specific choices made to adapt the beam-forming included:

- Using seismic stations outside the study area as virtual sources, to improve azimuthal coverage at the edge of the study area.
- Taking into account the short distances between the array and the "source" station. This was done mainly by assuming circular wavefronts following Maupin [2011] rather than plane wavefronts, and imposing a minimum distance between array and "source" station. The implementation still allowed to take into account great-circle deviations, which can be significant across AlpArray.
- Propagating uncertainty of each data point (phase velocity at a given period for a given array and source stations, see example in Figure 6f). This is done by weighting each observed phase velocity for the estimate of the A_2 and θ_2 terms for a given array at a given period, with the normalised beam amplitude $d_{\max}$, and use of bootstrap to estimate the uncertainty on A_2 and θ_2.
- Exclusion of data points if the isotropic bias (estimated by A_1) is significant.
- Adapting array geometry to wavelength and noise levels.

Figure 7 shows two examples of surface wave azimuthal anisotropy measured with this method across the Alpine area, at 15 s and 40 s period. Points with risk of a strong isotropic bias (high value of A_1 as compared to A_2, see Equation (1)) are excluded from the maps. In many points, the bias was particularly strong at periods which are sensitive to changes in Moho depth, and was overall coherent with areas of strong isotropic velocity gradients. For further discussion, we refer to Soergel et al. [2023].

The beamforming yields spatially coherent patterns of azimuthal anisotropy across all of the study area. Overall, the beamforming is in good agreement with the Eikonal method (Figure 5) on key findings,

such as (at 15 s period) lower amplitude anisotropy within the Alps as compared to surrounding areas, and the surrounding areas being dominated by chain parallel fast direction. There are main differences at the periphery of the study area, which can be explained by the lack of azimuthal coverage in the Eikonal tomography. Lateral smoothing effects are also different between the two methods. While the reliability of the beamforming is high due to the point by point (geographically, for each period) evaluation of quality and errors, it also leads to changing geographical distributions of reliable data with period, and the implementation would need to resolve this issue to be able to provide 3-D models of anisotropy.

Depth inversions for azimuthal anisotropy must be considered a priority in anisotropic studies because of the wide range of possible values of A_2. For example, if the upper crust is strongly anisotropic and neither lower crust or upper mantle are anisotropic, the observed anisotropy at, for example, 40 s period still has its origin in the upper crust. Similarly, changes in fast direction in layers with small anisotropy are not directly visible at any given period. Whether small amplitude anisotropy is resolved therefore strongly depends on the observation error. The strong control of errors provided by beamforming is consequently key for the depth inversions which are addressed in the following section.

3.2. *Transdimensional Bayesian inversions of anisotropic measurements*

Similar to isotropic inversions, once surface wave velocities have been estimated at different periods, they can be inverted to recover anisotropic shear wave velocity structure at depth. This is usually done in a second inversion step carried out at each geographical location. Rayleigh and Love dispersion curves can be jointly inverted for radial anisotropy parameters with depth. In the case of azimuthal anisotropy, Rayleigh and Love wave dispersion curves and their azimuthal dependency at each period can each be inverted to obtain azimuthal anisotropy parameters with depth.

Fortunately, this inverse problem is only weakly nonlinear, and many linearized approaches have been used, where data derivatives (sensitivity kernels) computed around a reference model are used. However, the solution is highly non-unique,
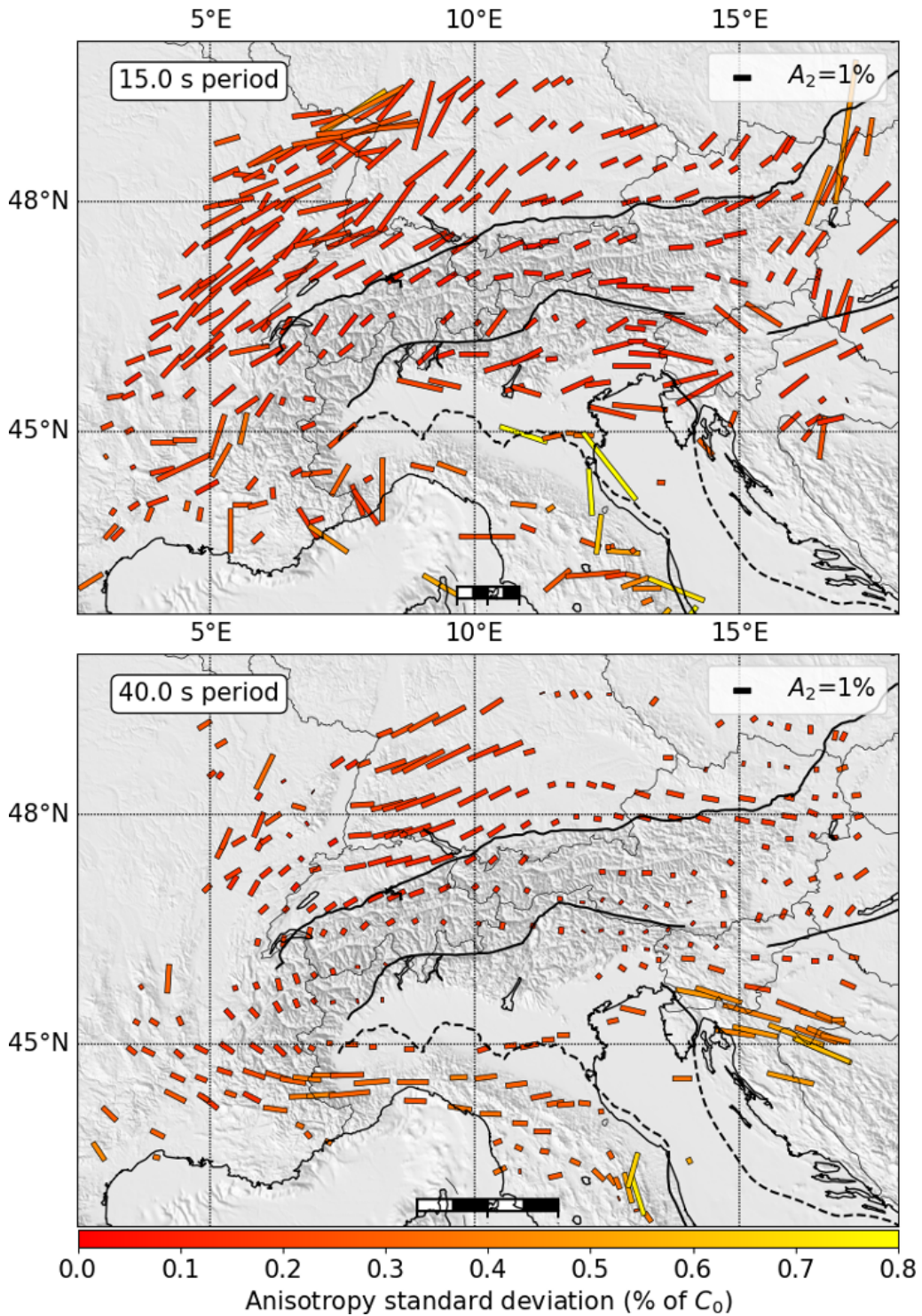
Figure 7. Maps of azimuthal anisotropy at 15 s and 40 s period resulting from the beamforming method. The direction of each line shows the fast direction, and the length shows the amplitude. The colour of the lines show the estimated uncertainty on the amplitude A_2 (in percent of C_0).

as surface waves are only sensitive to integrated velocities along a depth range. In the case where seismic anisotropy is inverted for, the non-uniqueness of the solution becomes particularly problematic as strong trade-offs emerge between different parameters. For example, the level of radial anisotropy trades off with V_p and with the level of heterogeneities in V_s [Bodin et al., 2015, Alder et al., 2017, Gao and Lekić, 2018], because of the equivalence of a stack of horizontal layers and a homogeneous anisotropic medium [Backus, 1962].

To add extra constraints on the solution, some regularisation can be used at the cost of biasing estimated uncertainties in the recovered model. In this way, linearized approaches only provide a unique velocity model that does not represent the range of potential solutions, and that is strongly dependent on the regularisation, the parameterization, or the reference model. For example, the V_p model is often set to a reference or arbitrarily scaled to V_s variations. The level of smoothness is also set in advance. Although these choices are based on geological or mineralogical arguments, they make the interpretation of results dependent on a priori choices.

Similar to isotropic inversions, these issues can be addressed by fully exploring the range of potential solutions with Monte Carlo methods (see Section 2.2.1). Since forward simulations are computationally cheap, a large number of 1-D models with variable parameterizations can be tested to sample complex posterior distributions. Adaptive parameterizations can be used to explore complex trade-offs between model parameters. For example, a transdimensional parameterization (where the number of model parameters is variable) can be used to explore the ambiguity between the level of spatial heterogeneity (horizontal layering) and the level of anisotropy created by the orientation of anisotropic minerals [Bodin et al., 2015, 2016, Alder et al., 2017]. In this case, the total number of layers in the inverted model as well as the presence of anisotropy in each layer are not constant parameters. Instead, they are adjusted by the inversion to fit the data to the degree required by their estimated noise. In this context, the Bayesian framework enables to propagate estimated uncertainties in the observed dispersion curves towards uncertainties in shear wave velocities at depth.

3.2.1. *Adaptive parameterizations: example with radial anisotropy*

To illustrate the benefit of such flexible parameterizations, we first show in Figure 8 an example of a synthetic test taken from Alder et al. [2021]. A target model is designed with a radially anisotropic layer in the crust and an isotropic upper crust and mantle. Noisy synthetic data are created and inverted with a transdimensional Monte Carlo algorithm, but with two different types of parameterizations (left and right panels). On the left, the number of layers is variable and each layer can be either isotropic and described solely by V_s and V_p (in this case, radial anisotropy in the form V_{SH}/V_{SV} takes a constant value of 1), or radially anisotropic and described by three parameters: V_{SV}, V_p and the level of radial anisotropy V_{SH}/V_{SV}. In this way, the number of inverted physical parameters in each layer is variable. On the right panel, the number of layers is also variable but all layers are radially anisotropic and described by three parameters. Everything else is equal in the two inversions.

Although the shear wave velocity is equally well resolved in both cases, the anisotropic layer in the crust is better recovered with the flexible scheme on the left. In the mantle, where the true model is isotropic, the ensemble solution produced on the left panel includes a large number of isotropic models, resulting in a narrower distribution for radial anisotropy and a median value of the distribution equal to unity. Conversely, in the case where anisotropy is imposed at all depths (right panels), a wider distribution of anisotropy is obtained, resulting in wider uncertainties.

This comparison shows that in the case of a true isotropic model, a flexible parameterization allows fitting data with simpler isotropic models that are described by fewer parameters. The result of the inversion is a distribution of models which is closer to the true model.

3.2.2. *Exploiting the full wealth of information in posterior distributions: example with azimuthal anisotropy*

The previous example shows the benefits of using complex adaptive parameterizations in Bayesian inversions. The solution is not a single model, but an ensemble of models with variable
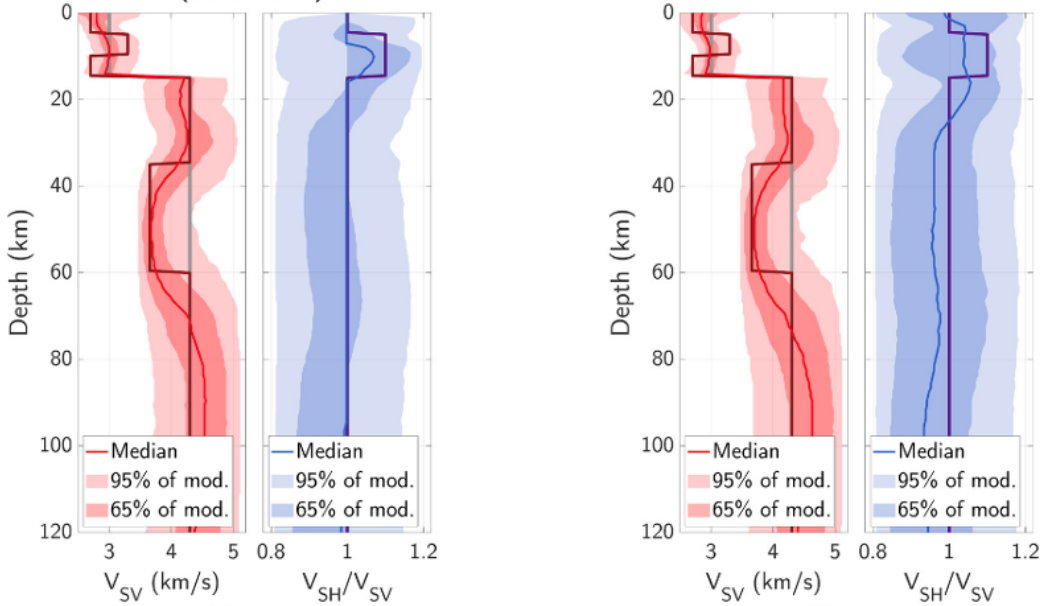
Figure 8. Joint inversion of Love and Rayleigh wave synthetic dispersion curves. The same data produced by the true model are inverted with two different procedures. Posterior distributions of V_{SV} (red), and V_{SH}/V_{SV} (blue). The true model used to create synthetic data is the thick solid line in every panel and the mean of the prior distribution used in the inversion is the grey line in the V_{SV} panel. Posterior distributions are depicted with their median (thin solid line) and likelihood intervals: for each parameter, the dark surface includes 65% of the models in the ensemble solution while the light area includes 95% of the models. Left panels: inversion used in Alder et al. [2021], where each layer can either be isotropic or anisotropic. Right panels: inversion where anisotropy is imposed as an unknown parameter at all depths. Modified from Alder et al. [2021].

parameterizations that approximates a probability distribution defined in a multiple dimensional space. As shown in Figure 8, one simple way to exploit this complex solution is to extract the mean or median value for a given parameter at each depth. Standard deviations can also be used, but more information is available about posterior covariances and trade-offs, and inference about these quantities can be hard to make. This wealth of information can be exploited through different angles of analysis and visualisation, each one giving additional insight to specific geophysical questions.

We illustrate this in Figure 9 where Rayleigh wave dispersion curves and their azimuthal variations measured from beamforming (see Section 3.1.3) are inverted at depth following the method of Bodin et al. [2016]. Here, the number of layers is variable and each layer is either isotropic and described solely by its isotropic shear-wave velocity, or azimuthally

anisotropic and described by three parameters: (1) the isotropic shear-wave velocity; (2) the peak to peak level of azimuthal anisotropy, and (3) the direction of the horizontal fast axis relative to the north [Romanowicz and Yuan, 2012].

Figure 9 shows an example of inversion of a set of beamforming measurements below the Dinarides (location: ~45.3°N–16.3°E). The ensemble solution is shown in the left panels, where the probability of a given amplitude range and direction range for shear-wave anisotropy is shown at each depth. However, this way of displaying the posterior distribution does not show correlations and trade-offs between anisotropy amplitude and direction. Such plots do not show whether the sampled profiles contain thin isotropic layers, thin layers with strong anisotropy, or thick layers with small anisotropy.

To extract some key features from this complex probabilistic solution, Soergel et al. [2023] proposed
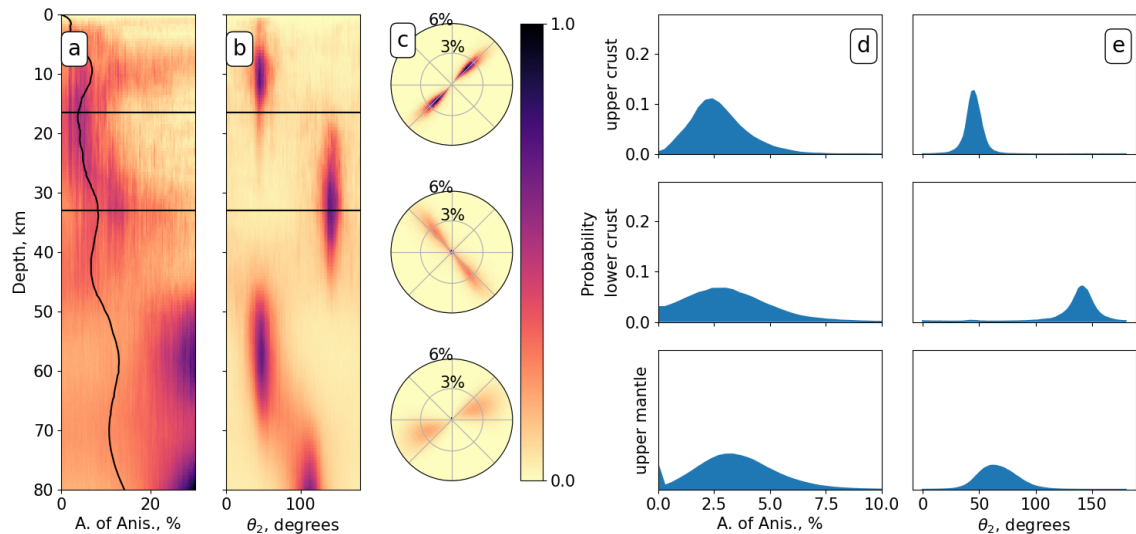
Figure 9. Depth inversion of Rayleigh wave surface wave dispersion curves with azimuthal variations for a subarray located in the Dinarides. The solution is a large ensemble of models with different parameterizations (different numbers of isotropic and anisotropic layers). (a) Probability distribution of the amplitude. (b) Probability distribution of the direction of the fast axis of anisotropy. The black line in (a) shows the average amplitude, and the horizontal black lines in (a) and (b) indicate the limits of the three layers over which we integrate anisotropy. (c) Density plot of anisotropy parameters integrated over the three different depth ranges. The radius in the polar plots indicate amplitude and the angle gives direction of the fast axis of anisotropy. The colour scale indicates the normalised probability of a given combination of amplitude and fast direction. Panels (d) and (e) show the marginal distributions of δV_s (d) and of θ_2 (e) for each of the three layers. The vertical scale is chosen such that the surface of the blue area is 1, that is the fraction of models with a given amplitude or (θ_2) range corresponds to the blue area within that range. Modified from Soergel et al. [2023].

to show the distribution of integrated anisotropy over a given depth range. The integration was defined as in Romanowicz and Yuan [2012], and carried out over three specific depth ranges with a meaningful sense (upper crust, lower crust, uppermost mantle). The distribution for the amplitude and direction of the anisotropy integrated over the three layers is shown in the right panels.

This visualisation makes it possible to see the correlations between fast direction and amplitude of anisotropy in each depth interval. Note that isotropic layers decrease the average level of anisotropy. Additionally, integrating anisotropy over several layers with different fast directions can also lead to anisotropy amplitudes smaller than expected. This explains the differences between the distribution of local anisotropy (left panels), and integrated anisotropy (right panels).

4. New information on the greater Alpine region

One of the main motivations behind the AlpArray initiative was to bring the resolution of seismic tomography closer to the spatial density of geological data over the entire Alpine belt, with the aim of increasing resolution of three-dimensional geological models at lithospheric scale. The methodological developments described in Section 2 have made a valuable contribution to this aim, in particular by providing new insights into the geometry of the crust-mantle boundary. A team of geologists and geophysicists is now working on exploiting the shear-wave velocity models derived by Nouibat et al. [2022a] and Nouibat et al. [2023] to build a 3-D structural model of the Western Alps [Bader et al., 2023]. All available geometrical (digital elevation model), geological (structural and geological maps) and geophysical

(3-D V_p and V_s models, DSS profiles, Moho models from seismic and gravity modeling/inversion, etc.) have been integrated and mixed in a geomodeling software, which provides a common framework and checks the geometrical coherence of geological interpretations of geophysical data [Calcagno et al., 2008]. The resolution of Nouibat et al. [2022a]'s model was sufficiently fine to allow Sonnet et al. [2023] to interpret a lateral V_s change in the subducted European lower crust as indication for the transition from amphibolite to granulite based on petrophysical data on Alpine rocks.

A depth map of the iso-velocity surface $V_s = 4.2$ km/s extracted from the model by Nouibat et al. [2023] is shown in Figure 10. As explained in Section 2.4, a composite depth map of velocity surfaces 3.8, 4.1 and 4.3 km/s would be a better proxy of the three Moho boundaries for the Ivrea body, the Ligurian basin, and Eurasia and Adria outside the Ivrea body region. The $V_s = 4.2$ km/s surface is therefore only an easy-to-calculate compromise. Since the velocity gradient is generally strong between 4.1 and 4.3 km/s, Figure 10 well illustrates lateral changes in Moho depth beneath the Alps revealed by our ambient noise tomography studies. The purple arrows highlight an ~8 km step in the European Moho with SSW–NNE orientation beneath the external crystalline massifs of the Western Alps, from Pelvoux to Mont Blanc. This orientation suggests that the Moho step might be a major lithospheric structure inherited from the Variscan orogeny. It had never been imaged before, even by the ECORS-CROP deep reflection profile, which showed reflections from the lower crust only west of the Belledonne external crystalline massif [e.g., Nicolas et al., 1990; see also Supplementary Figure S3 in Paul et al. [2022]]. The V_s models of Zhao et al. [2020], Nouibat et al. [2022a], and Nouibat et al. [2023] have confirmed the subduction of the European lithosphere beneath Adria, which is documented in Figure 10 by the dark blue areas (depth > 60 km). The CIFALPS cross-sections in Figures 3d–f document this continental subduction more precisely, with a European Moho reaching 75–80 km depth. Figure 10 also highlights the strong and rapid Moho depth changes along the belt strike, with maximum depths located right beneath the Insubric line (IL in Figure 10, also named Periadriatic fault further east) which marks the western and northern boundary of the undeformed Adria microplate

[Handy et al., 2010]. The 3-D detailed geometry and internal structure of the Ivrea body are also important new findings of our ambient noise tomography studies. For example, the "inverted Moho" highlighted by receiver function sections (InvM in Figure 3b, dotted thick grey line in Figure 3e) is explained by the overthrusting of the Ivrea mantle slice of Adriatic origin onto the lower velocity European crust. This boundary was imaged a few tens of km north of the CIFALPS line by wide-angle reflections of the ECORS-CROP complementary experiment [ECORS-CROP Deep Seismic Sounding Group, 1989]. It was interpreted as the top of a second mantle slice beneath the Ivrea body, while the polarity of converted signals in receiver function studies and ambient noise tomography studies have proven that this reflector is the base of the Ivrea body (single) mantle slice [Zhao et al., 2015, Paul et al., 2022].

In the Ligurian basin, the wave-equation ANT model with elastic–acoustic coupling by Nouibat et al. [2023] has provided new images of the basin margins and new estimates of sediment thickness with potential inferences on tectonic models of basin formation. On Ligurian Moho depth, the recently published ANT V_s model by Magrini et al. [2022] exhibits significant differences from the V_s model by Nouibat et al. [2022b], with 15–18 km crustal thickness along the basin axis in Magrini et al. [2022]'s model and 12 km in Nouibat et al. [2023]'s. As explained in Section 2.4, the thinner crust of Nouibat et al. [2022b] is fully consistent with the P-wave velocity model derived from the refraction-reflection profile LOBSTER-P02 of Dannowski et al. [2020] along the Ligurian basin axis. The difference in Moho depth estimates between Nouibat et al. [2022b, 2023] and Magrini et al. [2022] may be due to different ray coverages in the Ligurian basin, as Magrini et al. [2022] did not use AlpArray OBS data.

Very little information was available on the anisotropy of the crust and upper mantle beneath the Alpine region prior to the works described in Section 3. Kästle et al. [2022] and Soergel et al. [2023] have mapped azimuthal anisotropy of Rayleigh wave phase velocity using ambient noise records of the AASN and permanent seismic stations, and two different methods, Eikonal and beamforming. Their azimuthal anisotropy maps are broadly similar at all periods, except at the periphery of the study area, probably due to differences in ray coverage
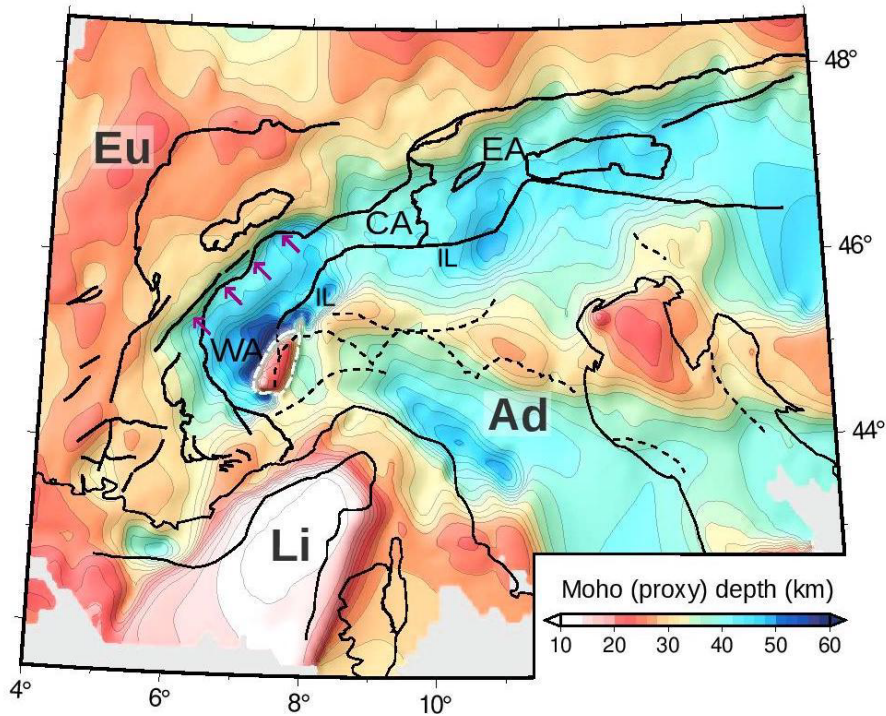
Figure 10. Depth map of the iso-velocity surface V_s = 4.2 km/s, extracted from the wave-equation ambient noise tomography model of Nouibat et al. [2023]. The continuous and dotted black lines are the main geological boundaries and faults, similar to Figure 1. The purple arrows highlight the Moho step located beneath the external crystalline massifs of the Western Alps. The dashed white line outlines the top of the high-velocity, peridotitic core of the Ivrea body, which appears as a dark blue spot in Figures 3d–f. Ad: Adria; CA: Central Alps; EA: Eastern Alps; Eu: Eurasia; IL: Insubric line; Li: Ligurian basin; WA: Western Alps. Modified from Nouibat et al. [2023].

(see examples at 15 and 40 s period in Figures 5 and 7). The Bayesian inversions for azimuthal anisotropy distribution with depth by Soergel et al. [2023] have shown that the anisotropic structure cannot be easily inferred from maps at individual periods. Spatially coherent anisotropy patterns are only visible in the upper half of the crust, with fast-velocity directions mostly parallel to the strike of the belt and amplitudes of 1–2% [see Figure 14 in Soergel et al., 2023]. By contrast, fast-velocity directions are mostly perpendicular to the belt in the lower half of the crust and uppermost mantle, with strongly varying amplitudes and no large-scale spatial pattern. This contrast between the shallow and deep layers suggests that Alpine deformation has only impacted the upper crust, through oriented crack and fractures, while the lower crust and upper mantle bear the imprint of more ancient processes. A single region located northwest of the Jura mountains displays coherent NE–SW fast velocity directions from the upper crust to the upper mantle, and rather strong amplitudes (~1%) in the lower crust. This orientation suggests that the observed anisotropy in that area outside the Alps may be of Variscan origin, and unaffected by the Alpine orogeny. Soergel et al. [2023] highlight the general disagreement between the fast-velocity directions they measured in the upper mantle and the fast directions measured from the splitting of core-refacted XKS teleseismic phases [e.g., Hein et al., 2021]. This may indicate that the source of XKS splitting is located deeper than the lithospheric mantle, either in the asthenosphere or in the subduction slabs.

When applied to Rayleigh and Love dispersion curves measured in the Alpine region, the flexible parameterization of Bayesian inversion allowed Alder et al. [2021] to produce maps of radial anisotropy differing from previous large-scale studies that suggested the presence of significant radial anisotropy everywhere in the European crust and shallow upper mantle [e.g., Zhu et al., 2015]. Instead, they observed that radial anisotropy is mostly localised beneath the Apennines while most of the crust and shallow upper mantle is isotropic in other parts of Europe. Thanks to synthetic tests, they attributed this difference to trade-offs between radial anisotropy and thin (hectometric) layering in previous studies based on least-squares inversions and long period data (>30 s). In contrast, Alder et al. [2021]'s approach involved a massive dataset of short period measurements and a Bayesian inversion that accounts for thin layering. They showed that the positive radial anisotropy ($V_{SH} > V_{SV}$) observed in the lower crust of the Apennines could not result from thin layering, but rather from ductile horizontal flow in response to the strong flexure of the Adriatic plate induced by doubly-vergent subduction.

5. Conclusions

The Alpine broadband seismic networks, including permanent stations and the temporary AlpArray seismic network have provided an optimal dataset for the development, improvement, and application of ambient-noise-based imaging methods. High station density and homogeneous coverage were key elements for these methodological improvements.

The overarching goals of our work were to improve observations when needed, move towards a probabilistic framework for inversion and interpretation, and adapting full waveform modelling in the forward problem. On the observational side, the work focused on (a) developing suitable techniques to combine OBS and land observations through higher order correlations, (b) improving our understanding of systematic errors made when measuring surface wave azimuthal anisotropy, and (c) applying and adapting beamforming techniques to seismic noise correlations to estimate surface wave anisotropy.

For the inversions, a Bayesian framework was applied both to 2-D inversions for group velocity maps [Nouibat et al., 2022a], and to 1-D depth inversions for elastic structure [Lu et al., 2018, Zhao et al., 2020, Alder et al., 2021, Soergel et al., 2023]. Particular efforts [Alder et al., 2021, Soergel et al., 2023] were made on the extraction of robust anisotropic parameters which are meaningful in a geologic/tectonic sense. Wave-equation ambient noise tomography studies by Lu et al. [2020] and Nouibat et al. [2023] have further improved ANT models by accounting for the physics of seismic wave propagation. The introduction of elastic–acoustic coupling at the seabed has enabled Nouibat et al. [2023] to improve the imaging of shallow layers below the sea. All of these developments led to improved models of the crust and uppermost mantle on the scale of the greater Alpine area (see Section 4).

The link between the overarching goals is naturally increasing because of the strong link between observational errors and the estimation of model resolution within a probabilistic inversion framework. In such a framework, the inversion provides not a single Earth model, but an ensemble of models obtained whilst taking into account uncertainties of inverted data. In this context, reliable error estimates of observables become objectively tied to the estimation of model uncertainties [Gallagher et al., 2009, Sambridge et al., 2013]. Also, the ensemble of models can be explored based on scientific questions (for example "What is the probability that the lower crust beneath the Apennines has significant radial anisotropy of crystallographic origin?") [Curtis, 1999, Meier et al., 2007, Zhang and Curtis, 2021].

Note also that the Bayesian framework allows to include independent information from geology, mineralogy, or other geophysical methods such as gravimetry. This can be done through the definition of the a priori distribution, or through the joint inversion of different datasets. Including other data types sensitive to P-wave structure (body waves) would be very useful for geological interpretation, as P and S waves have different sensitivities to different rock types, for example to hydrated minerals. In this context, full waveform inversion has the benefit to model the entire wavefield without having to preliminary extract and separate different data types (arrival times, phase velocities, splitting parameters, etc.), and three-dimensional variations of the entire elastic tensor can be directly reconstructed, including V_p, V_s and anisotropy. However, full waveform to-

mography in a fully non-linear Bayesian framework is still a prospect for the future, due to the computational cost of the forward model.

Within the framework of the AlpArray experiment, other noise-based methods were developed. For crustal imaging, it is becoming feasible to image coda-Q [Soergel et al., 2020], overcoming the difficulty of obtaining reliable amplitudes of noise correlations. This method makes it possible to estimate coda-Q at longer periods than those accessible through local earthquake estimates, but the method needs to be further developed to fully understand the meaning and reliability of the observed coda-Q values. The dense data coverage of the Alps also served the purpose of improving methods to extract body waves (reflections from mantle discontinuities) from seismic noise correlations [Pedersen et al., 2023, Lu et al., 2023].

The methods developed within the framework of the AlpArray experiment can naturally be applied and further improved within the framework of other dense and large-scale seismic arrays, such as the recently started AdriaArray experiment which significantly extends the area of high station density around the Adriatic plate, from the French Massif Central in the west to the Carpathians in the east [Kolínský et al., 2023; https://orfeus.readthedocs.io/en/latest/adria_array_main.html].

Declaration of interests

The authors do not work for, advise, own shares in, or receive funds from any organization that could benefit from this article, and have declared no affiliations other than their research organizations.

Funding

Acknowledgments

References

Aki, K., Christoffersson, A., and Husebye, E. S. (1977). Determination of the three-dimensional seismic structure of the lithosphere. *J. Geophys. Res.*, 82(2), 277–296.

Alder, C., Bodin, T., Ricard, Y., Capdeville, Y., Debayle, E., and Montagner, J. P. (2017). Quantifying seismic anisotropy induced by small-scale chemical heterogeneities. *Geophys. J. Int.*, 211(3), 1585–1600.

Alder, C., Debayle, E., Bodin, T., Paul, A., Stehly, L., Pedersen, H., and AlpArray Working Group (2021). Evidence for radial anisotropy in the lower crust of the Apennines from Bayesian ambient noise tomography in Europe. *Geophys. J. Int.*, 226(2), 941–967.

AlpArray Seismic Network (2014). Eastern Alpine Seismic Investigation (EASI)—AlpArray Complimentary Experiment [Data set]. AlpArray Working Group. https://doi.org/10.12686/alparray/xt_2014.

AlpArray Seismic Network (2015). AlpArray Seismic Network (AASN) temporary component [Data

set]. AlpArray Working Group. https://doi.org/10.12686/alparray/z3_2015.

Alvizuri, C. and Tanimoto, T. (2011). Azimuthal anisotropy from array analysis of Rayleigh waves in Southern California. *Geophys. J. Int.*, 186(3), 1135–1151.

Argand, E. (1922). La tectonique de l'Asie. In *Conference at the Geological International Congress XIII, Brussels (Belgium)*, pages 171–372. https://hal-insu.archives-ouvertes.fr/insu-00575289/.

Backus, G. E. (1962). Long-wave elastic anisotropy produced by horizontal layering. *J. Geophys. Res.*, 67(11), 4427–4440.

Bader, A. G., Calcagno, P., Bellahsen, N., and Paul, A. (2023). Towards a 3D crustal geomodel of the Western Alps in the French Geological Reference Platform (RGF). In *EGU General Assembly Conference Abstracts*, pages EGU–11633.

Bagagli, M., Molinari, I., Diehl, T., Kissling, E., and Giardini, D. (2022). The AlpArray research seismicity-catalogue. *Geophys. J. Int.*, 231(2), 921–943.

Barruol, G., Bonnin, M., Pedersen, H., Bokelmann, G. H., and Tiberi, C. (2011). Belt-parallel mantle flow beneath a halted continental collision: The Western Alps. *Earth Planet. Sci. Lett.*, 302(3–4), 429–438.

Barruol, G., Deschamps, A., and Coutant, O. (2004). Mapping upper mantle anisotropy beneath SE France by SKS splitting indicates Neogene asthenospheric flow induced by Apenninic slab roll-back and deflected by the deep Alpine roots. *Tectonophysics*, 394(1–2), 125–138.

Bodin, T., Capdeville, Y., Romanowicz, B., and Montagner, J. P. (2015). Interpreting radial anisotropy in global and regional tomographic models. In Khan, A. and Deschamps, F., editors, *The Earth's Heterogeneous Mantle*, Springer Geophysics, pages 105–144. Springer, Cham.

Bodin, T., Leiva, J., Romanowicz, B., Maupin, V., and Yuan, H. (2016). Imaging anisotropic layering with Bayesian inversion of multiple data types. *Geophys. J. Int.*, 206(1), 605–629.

Bodin, T., Sambridge, M., Rawlinson, N., and Arroucau, P. (2012). Transdimensional tomography with unknown data noise. *Geophys. J. Int.*, 189(3), 1536–1556.

Bokelmann, G., Qorbani, E., and Bianchi, I. (2013). Seismic anisotropy and large-scale deformation of the Eastern Alps. *Earth Planet. Sci. Lett.*, 383, 1–6.

Boschi, L. and Dziewonski, A. M. (1999). High- and low-resolution images of the Earth's mantle: Implications of different approaches to tomographic modeling. *J. Geophys. Res.: Solid Earth*, 104(B11), 25567–25594.

Boschi, L., Fry, B., Ekström, G., and Giardini, D. (2009). The European upper mantle as seen by surface waves. *Surv. Geophys.*, 30, 463–501.

Calcagno, P., Chilès, J. P., Courrioux, G., and Guillen, A. (2008). Geological modelling from field data and geological knowledge: Part I. Modelling method coupling 3d potential-field interpolation and geological rules. *Phys. Earth Planet. Inter.*, 171, 147–157.

Campillo, M. (2006). Phase and correlation in "random" seismic fields and the reconstruction of the green function. *Pure Appl. Geophys.*, 163, 475–502.

Campillo, M. and Paul, A. (2003). Long-range correlations in the diffuse seismic coda. *Science*, 299(5606), 547–549.

Chen, M., Huang, H., Yao, H., van der Hilst, R., and Niu, F. (2014). Low wave speed zones in the crust beneath SE Tibet revealed by ambient noise adjoint tomography. *Geophys. Res. Lett.*, 41(2), 334–340.

Chopin, C. (1984). Coesite and pure pyrope in high-grade blueschists of the Western Alps: A first record and some consequences. *Contrib. Mineral. Petrol.*, 86, 107–118.

Closs, H. and Labrouste, Y. (1963). *Recherches séismologiques dans les Alpes Occidentales au moyen des grandes explosions en 1956, 1958 et 1960: Année Géophysique Internationale*. CNRS. 12e série, fasc. II.

Crawford, W. C. and Webb, S. C. (2000). Identifying and removing tilt noise from low-frequency (<0.1 Hz) seafloor vertical seismic data. *Bull. Seismol. Soc. Am.*, 90(4), 952–963.

Crawford, W. C., Webb, S. C., and Hildebrand, J. A. (1998). Estimating shear velocities in the oceanic crust from compliance measurements by twodimensional finite difference modeling. *J. Geophys. Res.: Solid Earth*, 103(B5), 9895–9916.

Curtis, A. (1999). Optimal design of focused experiments and surveys. *Geophys. J. Int.*, 139(1), 205–215.

Dannowski, A., Kopp, H., Grevemeyer, I., Lange, D., Thorwart, M., Bialas, J., and Wollatz-Vogt, M. (2020). Seismic evidence for failed rifting in the Ligurian Basin, Western Alpine domain. *Solid Earth*,

11(3), 873–887.

Díaz, J., Gil, A., and Gallart, J. (2013). Uppermost mantle seismic velocity and anisotropy in the Euro-Mediterranean region from Pn and Sn tomography. *Geophys. J. Int.*, 192(1), 310–325.

Diehl, T., Husen, S., Kissling, E., and Deichmann, N. (2009). High-resolution 3-DP-wave model of the Alpine crust. *Geophys. J. Int.*, 179(2), 1133–1147.

ECORS-CROP Deep Seismic Sounding Group (1989). A new picture of the Moho under the western Alps. *Nature*, 337(6204), 249–251.

El-Sharkawy, A., Meier, T., Lebedev, S., Behrmann, J. H., Hamada, M., Cristiano, L., et al. (2020). The slab puzzle of the Alpine-Mediterranean region: Insights from a new, high-resolution, shear wave velocity model of the upper mantle. *Geochem. Geophys. Geosyst.*, 21(8), article no. e2020GC008993.

Eva, E., Malusà, M. G., and Solarino, S. (2015). A seismotectonic picture of the inner southern Western Alps based on the analysis of anomalously deep earthquakes. *Tectonophysics*, 661, 190–199.

Fichtner, A. (2014). Source and processing effects on noise correlations. *Geophys. J. Int.*, 197(3), 1527–1531.

Frei, W., Heitzmann, P., and Lehner, P. (1990). Swiss NFP-20 research program of the deep structure of the Alps. *Mémoires de la Société géologique de France (1833)*, 156, 29–46.

Friedrich, A., Krüger, F., and Klinge, K. (1998). Ocean-generated microseismic noise located with the Gräfenberg array. *J. Seismol.*, 2, 47–64.

Froment, B., Campillo, M., Roux, P., Gouedard, P., Verdel, A., and Weaver, R. L. (2010). Estimation of the effect of non-isotropically distributed energy on the apparent arrival time in correlations. *Geophysics*, 75(5), SA85–SA93.

Fry, B., Deschamps, F., Kissling, E., Stehly, L., and Giardini, D. (2010). Layered azimuthal anisotropy of Rayleigh wave phase velocities in the European Alpine lithosphere inferred from ambient noise. *Earth Planet. Sci. Lett.*, 297(1–2), 95–102.

Gallagher, K., Charvin, K., Nielsen, S., Sambridge, M., and Stephenson, J. (2009). Markov chain Monte Carlo (MCMC) sampling methods to determine optimal models, model resolution and model choice for Earth Science problems. *Mar. Pet. Geol.*, 26(4), 525–535.

Gao, C. and Lekić, V. (2018). Consequences of parametrization choices in surface wave inversion: Insights from transdimensional Bayesian methods. *Geophys. J. Int.*, 215(2), 1037–1063.

Grad, M., Tiira, T., and ESC Working Group (2009). The Moho depth map of the European Plate. *Geophys. J. Int.*, 176(1), 279–292.

Guerin, G., Rivet, D., Deschamps, A., Larroque, C., Mordret, A., Dessa, J. X., and Martin, X. (2020). High resolution ambient noise tomography of the Southwestern Alps and the Ligurian margin. *Geophys. J. Int.*, 220(2), 806–820.

Handy, M. R., Schmid, S. M., Bousquet, R., Kissling, E., and Bernoulli, D. (2010). Reconciling plate-tectonic reconstructions of Alpine Tethys with the geological–geophysical record of spreading and subduction in the Alps. *Earth-Sci. Rev.*, 102(3–4), 121–158.

Harmon, N., Rychert, C., and Gerstoft, P. (2010). Distribution of noise sources for seismic interferometry. *Geophys. J. Int.*, 183(3), 1470–1484.

Hein, G., Kolínský, P., Bianchi, I., and Bokelmann, G. (2021). Shear wave splitting in the Alpine region. *Geophys. J. Int.*, 227(3), 1996–2015.

Heit, B., Weber, M., Tilmann, F., Haberland, C., Jia, Y., Carraro, C., Walcher, G., Franceschini, A., and Pesaresi, D. (2017). The Swath-D Seismic Network in Italy and Austria [Data set]. GFZ Data Services. https://doi.org/10.14470/MF7562601148.

Hetényi, G., Molinari, I., Clinton, J., Bokelmann, G., Bondar, I., Crawford, W. C., et al. (2018a). The AlpArray seismic network: A large-scale European experiment to image the Alpine orogen. *Surv. Geophys.*, 39(5), 1009–1033.

Hetényi, G., Plomerová, J., Bianchi, I., Exnerová, H. K., Bokelmann, G., Handy, M. R., Babuška, V., and AlpArray-EASI Working Group (2018b). From mountain summits to roots: Crustal structure of the Eastern Alps and Bohemian Massif along longitude 13.3° E. *Tectonophysics*, 744, 239–255.

Juretzek, C. and Hadziioannou, C. (2016). Where do ocean microseisms come from? A study of Love-to-Rayleigh wave ratios. *J. Geophys. Res.: Solid Earth*, 121(9), 6741–6756.

Kästle, E. D., El-Sharkawy, A., Boschi, L., Meier, T., Rosenberg, C., Bellahsen, N., Cristiano, L., and Weidle, C. (2018). Surface wave tomography of the Alps using ambientnoise and earthquake phase velocity measurements. *J. Geophys. Res.: Solid Earth*, 123(2), 1770–1792.

Kästle, E. D., Molinari, I., Boschi, L., Kissling, E.,

and AlpArray Working Group (2022). Azimuthal anisotropy from eikonal tomography: example from ambient-noise measurements in the AlpArray network. *Geophys. J. Int.*, 229(1), 151–170.

Kästle, E. D., Soomro, R., Weemstra, C., Boschi, L., and Meier, T. (2016). Two-receiver measurements of phase velocity: cross-validation of ambient-noise and earthquake-based observations. *Geophys. J. Int.*, 207(3), 1493–1512.

Kästle, E. D., Tilmann, F., and AlpArray and Swath-D Working Groups (2024). Anisotropic reversible-jump McMC shear-velocity tomography of the Eastern Alpine crust. *Geochem. Geophys. Geosyst.*, 25(3), article no. e2023GC011238.

Kolínský, P., Meier, T., and AdriaArray Seismology Group (2023). AdriaArray Seismic Network – status in April 2023. In *EGU General Assembly*, pages EGU23–12284.

Komatitsch, D. and Tromp, J. (1999). Introduction to the spectral element method for three-dimensional seismic wave propagation. *Geophys. J. Int.*, 139(3), 806–822.

Komatitsch, D. and Vilotte, J. P. (1998). The spectral element method: an efficient tool to simulate the seismic response of 2D and 3D geological structures. *Bull. Seismol. Soc. Am.*, 88(2), 368–392.

Kummerow, J., Kind, R., Oncken, O., Giese, P., Ryberg, T., Wylegalla, K., Scherbaum, F., and TRANSALP Working Group (2004). A natural and controlled source seismic profile through the Eastern Alps: TRANSALP. *Earth Planet. Sci. Lett.*, 225, 115–129.

Kustowski, B., Ekström, G., and Dziewoński, A. M. (2008). Anisotropic shearwave velocity structure of the Earth's mantle: A global model. *J. Geophys. Res.: Solid Earth*, 113(B6), article no. B06306.

Kvapil, J., Plomerová, J., Kampfová Exnerová, H., Babuška, V., Hetényi, G., and AlpArray Working Group (2021). Transversely isotropic lower crust of Variscan central Europe imaged by ambient noise tomography of the Bohemian Massif. *Solid Earth*, 12(5), 1051–1074.

Landès, M., Hubans, F., Shapiro, N. M., Paul, A., and Campillo, M. (2010). Origin of deep ocean microseisms by using teleseismic body waves. *J. Geophys. Res.: Solid Earth*, 115(B5), article no. B05302.

Lin, F. C. and Ritzwoller, M. H. (2011). Apparent anisotropy in inhomogeneous isotropic media. *Geophys. J. Int.*, 186(3), 1205–1219.

Lin, F. C., Ritzwoller, M. H., and Snieder, R. (2009).

Eikonal tomography: surface wave tomography by phase front tracking across a regional broad-band seismic array. *Geophys. J. Int.*, 177(3), 1091–1110.

Lippitsch, R., Kissling, E., and Ansorge, J. (2003). Upper mantle structure beneath the Alpine orogen from high-resolution teleseismic tomography. *J. Geophys. Res.*, 108(B8), article no. 2376.

Lombardi, D., Braunmiller, J., Kissling, E., and Giardini, D. (2008). Moho depth and Poisson's ratio in the Western-Central Alps from receiver functions. *Geophys. J. Int.*, 173(1), 249–264.

Lu, Y., Schmid, S. M., Wang, Q. Y., and Bokelmann, G. (2023). Mapping the mantle transition zone discontinuities across South-Central Europe using body waves from seismic noise correlations. *Earth Planet. Sci. Lett.*, 624, article no. 118457.

Lu, Y., Stehly, L., Brossier, R., Paul, A., and AlpArray Working Group (2020). Imaging Alpine crust using ambient noise wave-equation tomography. *Geophys. J. Int.*, 222(1), 69–85.

Lu, Y., Stehly, L., Paul, A., and AlpArray Working Group (2018). High-resolution surface wave tomography of the European crust and uppermost mantle from ambient seismic noise. *Geophys. J. Int.*, 214(2), 1136–1150.

Lucente, F. P., Margheriti, L., Piromallo, C., and Barruol, G. (2006). Seismic anisotropy reveals the long route of the slab through the western-central Mediterranean mantle. *Earth Planet. Sci. Lett.*, 241(3–4), 517–529.

Lüschen, E., Borrini, D., Gebrande, H., Lammerer, B., Millahn, K., Neubauer, F., Nicolich, R., and TRANSALP Working Group (2006). TRANSALP—deep crustal Vibroseis and explosive seismic profiling in the Eastern Alps. *Tectonophysics*, 414, 9–38.

Macquet, M., Paul, A., Pedersen, H. A., Villaseñor, A., Chevrot, S., Sylvander, M., Wolyniec, D., and Pyrope Working Group (2014). Ambient noise tomography of the Pyrenees and the surrounding regions: inversion for a 3-D Vs model in the presence of a very heterogeneous crust. *Geophys. J. Int.*, 199(1), 402–415.

Magrini, F., Diaferia, G., El-Sharkawy, A., Cammarano, F., van Der Meijde, M., Meier, T., and Boschi, L. (2022). Surface-wave tomography of the central-western mediterranean: new insights into the liguro-provençal and tyrrhenian basins. *J. Geophys. Res.: Solid Earth*, 127(3), arti-

cle no. e2021JB023267.

Malusà, M. G., Guillot, S., Zhao, L., Paul, A., Solarino, S., Dumont, T., et al. (2021). The deep structure of the Alps based on the CIFALPS seismic experiment: A synthesis. *Geochem. Geophys. Geosyst.*, 22(3), article no. e2020GC009466.

Marchant, R. H. and Stampfli, G. M. (1997). Subduction of continental crust in the Western Alps. *Tectonophysics*, 269(3–4), 217–235.

Mauerberger, A., Maupin, V., Gudmundsson, Ó., and Tilmann, F. (2021). Anomalous azimuthal variations with 360° periodicity of Rayleigh phase velocities observed in Scandinavia. *Geophys. J. Int.*, 224(3), 1684–1704.

Maupin, V. (2011). Upper-mantle structure in southern Norway from beamforming of Rayleigh wave data presenting multipathing. *Geophys. J. Int.*, 185(2), 985–1002.

Maupin, V. and Park, J. (2015). 1.09—Theory and observations—Seismic anisotropy. In *Treatise on Geophysics*, volume 20, pages 277–305. Elsevier, Amsterdam.

Meier, U., Curtis, A., and Trampert, J. (2007). Global crustal thickness from neural network inversion of surface wave data. *Geophys. J. Int.*, 169(2), 706–722.

Michailos, K., Hetényi, G., Scarponi, M., Stipčević, J., Bianchi, I., Bonatto, L., others, and AlpArray-PACASE Working Group (2023). Moho depths beneath the European Alps: a homogeneously processed map and receiver functions database. *Earth Syst. Sci. Data*, 15(5), 2117–2138.

Molinari, I., Obermann, A., Kissling, E., Hetényi, G., Boschi, L., and AlpArray-Easi Working Group (2020). 3D crustal structure of the Eastern Alpine region from ambient noise tomography. *Results Geophys. Sci.*, 1, article no. 100006.

Molinari, I., Verbeke, J., Boschi, L., Kissling, E., and Morelli, A. (2015). Italian and Alpine three-dimensional crustal structure imaged by ambient-noise surface-wave dispersion. *Geochem. Geophys. Geosyst.*, 16(12), 4405–4421.

Montagner, J. P. and Nataf, H. C. (1986). A simple method for inverting the azimuthal anisotropy of surface waves. *J. Geophys. Res.: Solid Earth*, 91(B1), 511–520.

Nicolas, A., Hirn, A., Nicolich, R., Polino, R., and ECORS-CROP Working Group (1990). Lithospheric wedging in the western Alps inferred from the ECORS-CROP traverse. *Geology*, 18, 587–590.

Nita, B., Maurya, S., and Montagner, J. P. (2016). Anisotropic tomography of the European lithospheric structure from surface wave studies. *Geochem. Geophys. Geosyst.*, 17(6), 2015–2033.

Nouibat, A., Brossier, R., Stehly, L., Cao, J., Paul, A., and AlpArray Working Group (2023). Ambient-noise wave-equation tomography of the Alps and Ligurian-Provence basin. *J. Geophys. Res.: Solid Earth*, 128, article no. e2023JB026776.

Nouibat, A., Stehly, L., Paul, A., Schwartz, S., Bodin, T., Dumont, T., Rolland, Y., Brossier, R., and AlpArray Working Group (2022a). Lithospheric transdimensional ambient-noise tomography of W-Europe: implications for crustal-scale geometry of the W-Alps. *Geophys. J. Int.*, 229(2), 862–879.

Nouibat, A., Stehly, L., Paul, A., Schwartz, S., Rolland, Y., Dumont, T., Crawford, W. C., Brossier, R., and AlpArray Working Group (2022b). Ambientnoise tomography of the Ligurian-Provence Basin using the AlpArray onshore-offshore network: Insights for the oceanic domain structure. *J. Geophys. Res.: Solid Earth*, 127, article no. e2022JB024228.

Paffrath, M., Friederich, W., Schmid, S. M., Handy, M. R., and AlpArray and AlpArray-Swath D Working Group (2021). Imaging structure and geometry of slabs in the greater Alpine area–A P-wave travel-time tomography using AlpArray Seismic Network data. *Solid Earth*, 12(11), 2671–2702.

Palano, M. (2015). On the present-day crustal stress, strain-rate fields and mantle anisotropy pattern of Italy. *Geophys. J. Int.*, 200(2), 969–985.

Pasyanos, M. E., Masters, T. G., Laske, G., and Ma, Z. (2014). LITHO1. 0: An updated crust and lithospheric model of the Earth. *J. Geophys. Res.: Solid Earth*, 119(3), 2153–2173.

Paul, A., Cattaneo, M., Thouvenot, F., Spallarossa, D., Béthoux, N., and Fréchet, J. (2001). A three-dimensional crustal velocity model of the southwestern Alps from local earthquake tomography. *J. Geophys. Res.: Solid Earth*, 106(B9), 19367–19389.

Paul, A., Malusà, M. G., Solarino, S., Salimbeni, S., Eva, E., Nouibat, A., et al. (2022). Along-strike variations in the fossil subduction zone of the Western Alps revealed by the CIFALPS seismic experiments and their implications for exhumation of (ultra-) high-pressure rocks. *Earth Planet. Sci. Lett.*, 598, article no. 117843.

Pedersen, H. A., Boué, P., Poli, P., and Colombi, A. (2015). Arrival angle anomalies of Rayleigh waves

observed at a broadband array: a systematic study based on earthquake data, full waveform simulations and noise correlations. *Geophys. J. Int.*, 203(3), 1626–1641.

Pedersen, H. A., Bruneton, M., Maupin, V., and SVEKALAPKO Seismic Tomography Working Group (2006). Lithospheric and sublithospheric anisotropy beneath the Baltic shield from surface-wave array analysis. *Earth Planet. Sci. Lett.*, 244(3–4), 590–605.

Pedersen, H. A., Mattern, F., Poli, P., and Stehly, L. (2023). Imaging with seismic noise: improving extraction of body wave phases from the deep Earth through selective stacking based on H/V ratios. *Geophys. J. Int.*, 232(2), 1455–1467.

Pilia, S., Rawlinson, N., Cayley, R. A., Bodin, T., Musgrave, R., Reading, A. M., Direen, N. G., and Young, M. K. (2015). Evidence of micro-continent entrainment during crustal accretion. *Sci. Rep.*, 5(1), article no. 8218.

Piromallo, C. and Morelli, A. (2003). P wave tomography of the mantle under the Alpine-Mediterranean area. *J. Geophys. Res.*, 108(B2), article no. 2065.

Qorbani, E., Bianchi, I., and Bokelmann, G. (2015). Slab detachment under the Eastern Alps seen by seismic anisotropy. *Earth Planet. Sci. Lett.*, 409, 96–108.

Rappisi, F., VanderBeek, B. P., Faccenda, M., Morelli, A., and Molinari, I. (2022). Slab geometry and upper mantle flow patterns in the central mediterranean from 3D anisotropic P-wave tomography. *J. Geophys. Res.: Solid Earth*, 127(5), article no. e2021JB023488.

Rawlinson, N. and Sambridge, M. (2004). Multiple reflection and transmission phases in complex layered media using a multistage fast marching method. *Geophysics*, 69(5), 1338–1350.

Riahi, N. and Saenger, E. H. (2014). Rayleigh and Love wave anisotropy in Southern California using seismic noise. *Geophys. Res. Lett.*, 41(2), 363–369.

Rollet, N., Déverchère, J., Beslier, M. O., Guennoc, P., Réhault, J. P., Sosson, M., and Truffert, C. (2002). Back arc extension, tectonic inheritance, and volcanism in the Ligurian Sea, Western Mediterranean. *Tectonics*, 21(3), 6–1–6–23.

Romanowicz, B. and Yuan, H. (2012). On the interpretation of SKS splitting measurements in the presence of several layers of anisotropy. *Geophys. J. Int.*, 188(3), 1129–1140.

Rost, S. and Thomas, C. (2002). Array seismology: Methods and applications. *Rev. Geophys.*, 40(3), 2–1–2–27.

Sadeghi-Bagherabadi, A., Vuan, A., Aoudia, A., Parolai, S., and AlpArray and AlpArray-Swath-D Working Group (2021). High-resolution crustal S-wave velocity model and Moho geometry beneath the Southeastern Alps: New insights from the SWATH-D experiment. *Front. Earth Sci.*, 9, article no. 641113.

Sager, K., Ermert, L., Boehm, C., and Fichtner, A. (2018). Towards full waveform ambient noise inversion. *Geophys. J. Int.*, 212(1), 566–590.

Salimbeni, S., Malusà, M. G., Zhao, L., Guillot, S., Pondrelli, S., Margheriti, L., et al. (2018). Active and fossil mantle flows in the western Alpine region unravelled by seismic anisotropy analysis and high-resolution P wave tomography. *Tectonophysics*, 731, 35–47.

Sambridge, M., Bodin, T., Gallagher, K., and Tkalčić, H. (2013). Transdimensional inference in the geosciences. *Phil. Trans. R. Soc. A*, 371(1984), article no. 20110547.

Schippkus, S., Zigone, D., and Bokelmann, G. (2020). Azimuthal anisotropy in the wider Vienna basin region: a proxy for the present-day stress field and deformation. *Geophys. J. Int.*, 220(3), 2056–2067.

Schippkus, S., Zigone, D., Bokelmann, G., and AlpArray Working Group (2018). Ambient-noise tomography of the wider Vienna Basin region. *Geophys. J. Int.*, 215(1), 102–117.

Schivardi, R. and Morelli, A. (2011). EPmantle: a 3-D transversely isotropic model of the upper mantle under the European Plate. *Geophys. J. Int.*, 185(1), 469–484.

Sénéchal, G. and Thouvenot, F. (1991). Geometrical migration of line-drawings: A simplified method applied to ECORS data. In *Continental Lithosphere: Deep Seismic Reflections*, volume 22 of *Geodynamics Series*, pages 401–407. American Geophysical Union, Washnigton DC.

Shapiro, N. M. and Campillo, M. (2004). Emergence of broadband Rayleigh waves from correlations of the ambient seismic noise. *Geophys. Res. Lett.*, 31(7), article no. L07614.

Shapiro, N. M., Campillo, M., Stehly, L., and Ritzwoller, M. H. (2005). High-resolution surface-wave tomography from ambient seismic noise. *Science*, 307(5715), 1615–1618.

Soergel, D., Pedersen, H. A., Stehly, L., Margerin, L., Paul, A., and AlpArray Working Group (2020). Coda-Q in the 2.5–20 s period band from seismic noise: application to the greater Alpine area. *Geophys. J. Int.*, 220(1), 202–217.

Soergel, S., Pedersen, H. A., Bodin, T., Paul, A., Stehly, L., and AlpArray Working Group (2023). Bayesian analysis of azimuthal anisotropy in the Alpine lithosphere from beamforming of ambient noise cross-correlations. *Geophys. J. Int.*, 232(1), 429–450.

Solarino, S., Kissling, E., Sellami, S., Smriglio, G., Thouvenot, F., Granet, M., Bonjer, K. P., and Sleijko, D. (1997). Compilation of a recent seismicity data base of the greater Alpine region from several seismological networks and preliminary 3D tomographic results. *Annali di Geofisica*, 40(1), 161–174.

Solarino, S., Malusà, M. G., Eva, E., Guillot, S., Paul, A., Schwartz, S., et al. (2018). Mantle wedge exhumation beneath the Dora-Maira (U)HP dome unravelled by local earthquake tomography (Western Alps). *Lithos*, 296, 623–636.

Sonnet, M., Labrousse, L., Bascou, J., Plunder, A., Nouibat, A., and Paul, A. (2023). Assessing chemical and mineralogical properties of the Alpine slab based on field analogues and ambient noise tomography. *Geochem. Geophys. Geosyst.*, 24, article no. e2022GC010784.

Spada, M., Bianchi, I., Kissling, E., Agostinetti, N. P., and Wiemer, S. (2013). Combining controlled-source seismology and receiver function information to derive 3-D Moho topography for Italy. *Geophys. J. Int.*, 194(2), 1050–1068.

Stehly, L., Fry, B., Campillo, M., Shapiro, N. M., Guilbert, J., Boschi, L., and Giardini, D. (2009). Tomography of the Alpine region from observations of seismic ambient noise. *Geophys. J. Int.*, 178(1), 338–350.

Szanyi, G., Gráczer, Z., Balázs, B., Kovács, I. J., and AlpArray Working Group (2021). The transition zone between the Eastern Alps and the Pannonian basin imaged by ambient noise tomography. *Tectonophysics*, 805, article no. 228770.

Trinh, P. T., Brossier, R., Métivier, L., Tavard, L., and Virieux, J. (2019). Efficient time-domain 3D elastic and viscoelastic full-waveform inversion using a spectral-element method on flexible Cartesian-based mesh. *Geophysics*, 84(1), R61–R83.

Tromp, J., Tape, C., and Liu, Q. (2005). Seismic tomography, adjoint methods, time reversal and banana-doughnut kernels. *Geophys. J. Int.*, 160(1), 195–216.

Verbeke, J., Boschi, L., Stehly, L., Kissling, E., and Michelini, A. (2012). High-resolution Rayleigh-wave velocity maps of central Europe from a dense ambient-noise data set. *Geophys. J. Int.*, 188(3), 1173–1187.

Virieux, J., Paul, A., Langlais, M., Janex, G., Guéguen, P., Helmstetter, A., and Stehly, L. (2024). Assessing the reliability of local earthquake tomography for crustal imaging: 30 years of records in the Western Alps as a case study. *Geophys. J. Int.*, 236(1), 99–118.

Waldhauser, F., Kissling, E., Ansorge, J., and Mueller, S. (1998). Three dimensional interface modelling with two-dimensional seismic data: the Alpine crust-mantle boundary. *Geophys. J. Int.*, 135(1), 264–278.

Waldhauser, F., Lippitsch, R., Kissling, E., and Ansorge, J. (2002). High-resolution teleseismic tomography of upper-mantle structure using an a priori three-dimensional crustal model. *Geophys. J. Int.*, 150(2), 403–414.

Weidle, C. and Maupin, V. (2008). An upper-mantle S-wave velocity model for Northern Europe from Love and Rayleigh group velocities. *Geophys. J. Int.*, 175(3), 1154–1168.

Wu, X., Guo, Z., Li, S., Yu, Y., Bai, Q., and Chen, Y. J. (2023). Seismic azimuthal anisotropy of northeastern Tibetan Plateau from ambient noise double beamforming tomography: Implication for crustal deformation. *J. Geophys. Res.: Solid Earth*, 128, article no. e2022JB026109.

Young, M. K., Rawlinson, N., and Bodin, T. (2013). Transdimensional inversion of ambient seismic noise for 3D shear velocity structure of the Tasmanian crust. *Geophysics*, 78(3), WB49–WB62.

Yuan, H. and Bodin, T. (2018). A probabilistic shear wave velocity model of the crust in the central West Australian craton constrained by transdimensional inversion of ambient noise dispersion. *Tectonics*, 37(7), 1994–2012.

Zahorec, P., Papčo, J., Pašteka, R., Bielik, M., Bonvalot, S., Braitenberg, C., et al. (2021). The first pan-Alpine surface-gravity database, a modern compilation that crosses frontiers. *Earth Syst. Sci. Data*, 13(5), 2165–2209.

Zhang, X. and Curtis, A. (2021). Bayesian geophysical inversion using invertible neural net-

works. *J. Geophys. Res.: Solid Earth*, 126(7), article no. e2021JB022320.

Zhao, L., Malusà, M. G., Yuan, H., Paul, A., Guillot, S., Lu, Y., et al. (2020). Evidence for a serpentinized plate interface favouring continental subduction. *Nat. Commun.*, 11(1), article no. 2171.

Zhao, L., Paul, A., Guillot, S., Solarino, S., Malusà, M. G., Zheng, T., Aubert, C., Salimbeni, S., Dumont, T., Schwartz, S., Zhu, R., and Wang, Q. (2015). First seismic evidence for continental subduction beneath the Western Alps. *Geology*, 43(9), 815–818.

Zhao, L., Paul, A., Malusà, M. G., Xu, X., Zheng, T., Solarino, S., et al. (2016a). Continuity of the Alpine slab unraveled by high-resolution P wave tomography. *J. Geophys. Res.: Solid Earth*, 121(12), 8720–8737.

Zhao, L., Paul, A., Solarino, S., and RESIF (2016b). Seismic network YP: CIFALPS temporary experiment (China-Italy-France Alps seismic transect) [Data set]. RESIF—Réseau Sismologique et géodésique Français. https://doi.org/10.15778/RESIF.YP2012.

Zhao, L., Paul, A., Solarino, S., and RESIF (2018). Seismic network XT: CIFALPS-2 temporary experiment (China-Italy-France Alps seismic transect #2) [Data set]. RESIF—Réseau Sismologique et géodésique Français. https://doi.org/10.15778/RESIF.XT2018.

Zhu, H., Bozdağ, E., and Tromp, J. (2015). Seismic structure of the European upper mantle based on adjoint tomography. *Geophys. J. Int.*, 201(1), 18–52.